Lettieri, A., de La Peña, A., Freddi, F., Latour, M. (2023). Damage-free self-centring link for eccentrically braced frames: development and numerical study. Journal of Constructional Steel Research, Special Issue on 'Seismic Resilient Steel Structures', 201: 107727. https://doi.org/10.1016/j.jcsr.2022.107727

Damage-free self-centring links for eccentrically braced frames: development and numerical study

Annarosa Lettieri[1, *], **Amparo de la Peña**[1], **Fabio Freddi**[2], **Massimo Latour**[1]

[1] *Department of Civil Engineering, University of Salerno, Salerno, Italy*
[2]*Department of Civil, Environmental & Geomatic Engineering, University College London, London, UK*
[*]Corresponding Author. *E-mail address:* alettieri@unisa.it

Abstract

Many recent research studies focused on the development of innovative seismic-resilient structures, chasing the objectives of minimising both seismic damage and repair time, hence allowing the definition of structures able to go back to the undamaged, fully functional condition in a short time. Steel seismic-resilient structures have been widely investigated in the past few years while considering solutions based on moment-resisting and concentrically braced frames. While the first category may be characterised by low stiffness, the second category is often characterised by low ductility. Conversely, eccentrically braced frames (EBFs) represent a compromise between the two and allow both strength and stiffness to be optimised while providing 'good' ductility capacity. The present study investigates a solution for damage-free self-centring EBFs relying on damage-free self-centring devices as seismic links (SC-links). The SC-links are based on post-tensioned high-strength steel bars with disk springs to provide the self-centring behaviour, and friction dampers to dissipate the seismic energy. Analytical equations governing the global behaviour of the connection are developed. A four-storey EBF complying with Eurocode 8 provisions is designed with conventional seismic links and upgraded with the proposed SC-link. The third storey of the structure is extracted to develop refined 3-D finite element (FE) models in ABAQUS. The results of the FE simulations are used to investigate the local behaviour of the seismic device and validate the accuracy of the analytical predictions. Moreover, a simplified 2-D FE model is developed in OpenSees to carry out Incremental Dynamic Analysis providing information on the global response of the structure. Residual and peak interstorey drifts and link rotations are monitored as Engineering Demand Parameters, and the seismic performances of the frames are compared.

Keywords: Steel Structures, Residual Drifts, Eccentrically Braced Frames, Damage-Free Self-Centring Links, Structural Resilience, Seismic Design.

1. INTRODUCTION

The design philosophy implemented in modern seismic design codes [*e.g.*, 1, 2] is based on the dissipation of the seismic input energy through the controlled damage of 'some' ductile structural components following the 'capacity design' approach. These components are properly detailed in order to sustain large inelastic deformations (*i.e.*, ductile behaviour) with limited strength and stiffness degradation. However, despite the energy dissipation capacity of the structures allows preventing the collapse of buildings subjected to 'rare' seismic events, it may result in significant direct (*e.g.*, casualties, repair cost) and indirect (*e.g.*, business interruption) losses [*e.g.*, 3, 4]. Besides, plastic deformations in the structural components often result in large residual drifts, significantly compromising building reparability [5]. Several research efforts proposed and investigated innovative seismic-resilient structural systems to control the structural damage and enable improvements in their self-centring capabilities [*e.g.*, 6-9]. Many of these studies focused on the development of self-centring moment-resisting frames (MRFs) [*e.g.*, 10-23] and concentrically braced frames (CBF) [*e.g.*, 24-30] by employing a combination of high-strength post-tensioned (PT) steel bars (or strands) to promote the self-centring capability of the structure, and dedicated fuses, *e.g.*, yielding or friction devices (FDs), to dissipate the seismic input energy. Additionally, other proposals improve the seismic performance of steel MRFs employing shape memory alloys (SMA) connections to restore the deformations and ductile energy dissipation links [22, 23]. Conversely, only a few studies focused on the development of seismic-resilient self-centring eccentrically braced frames (EBFs).

EBFs have been proposed, since the 1970s, as lateral force resisting systems able to combine the main advantages of MRFs and CBFs [*e.g.*, 31-35], providing the structure with a balanced stiffness, strength and ductility capacity. MRFs and CBFs dissipate the seismic energy by developing plastic hinges at beams' ends and within braces, respectively [36-37]. Conversely, EBFs dissipate the seismic input energy by developing plastic deformations in a segment of the beams denoted as 'seismic link' (or simply 'link'), while the other structural elements (*i.e.*, columns and braces) are properly over-strengthened. If properly designed, EBFs exhibit significant ductile deformations during strong seismic events, and the observations of their performances after recent seismic events showed that these structures performed well in preventing collapse [38]. Nevertheless, structural damage is unavoidable.

In the last decades, a few innovative systems for EBFs have been proposed with the aim of minimising structural damage, service disruption, and repair costs. Among others, several replaceable links for EBFs have been proposed. Stratan *et al.* [39] investigated EBFs with replaceable horizontal links. The authors studied a bolted connection with flush end-plates and high-strength bolts between links and beams to facilitate the replacement of damaged links after moderate to strong seismic events. Subsequently, several other replaceable links have been presented, including web-connected

links [40-41] and links with direct brace attachments [42]. Bozkur *et al*. [43] proposed another detachable replaceable link based on splicing the link at its mid-length. This solution uses standard end-plates at the mid-splice connection and gusseted joints to connect the bracings.

Although concentrating plastic deformations in replaceable elements is one of the main requirements to easily repair structures after earthquakes, successful replacement procedures can be implemented only if the structures' residual deformations (*i.e.*, residual drifts) are limited. In fact, residual drifts result in a misalignment of the collector beams' ends which may not allow the replacement of the links. McCormick *et al.* [5] suggested a residual drift equal to 0.5% as the threshold value beyond which the repairability of the structure may be compromised. Similarly, FEMA P-58 [44] suggests two damage states, *i.e.*, Damage State 1 (DS1) and 2 (DS2), with assigned residual drift thresholds, respectively, equal to 0.2% and 0.5%. DS1 and DS2 correspond respectively to damage conditions where structures can be repaired without the need for realignment and to situations beyond which the repairability of the structure may not be economically convenient.

For this reason, alternative strategies to replaceable links, such as self-centring steel structural systems, have been developed over the past few decades. Several research activities have focused on the use of dual configurations by combining EBFs with removable links and elastic MRFs to prevent excessive residual drifts [*e.g.*, 45-46]. In these systems, the elastic response of the MRFs provides the restoring forces to reduce residual displacements and facilitate the residual drift reduction during the reparation process. Further studies have been focused on self-centring systems for EBFs using elastic gap-opening mechanisms at beam-to-link [47] or beam-to-column interfaces [48,49] to re-centre the frame, in combination with energy dissipation devices. Among others, Cheng *et al*. [47] proposed and experimentally investigated a self-centring rocking link for EBFs. In this system, the rocking motion is developed between the link and adjacent beams and is controlled by post-tensioned strands providing the self-centring behaviour, while frictional hinge dampers are installed to increase the energy dissipation capacity. Tong *et al*. [48] experimentally investigated a D-type self-centring EBF composed of post-tensioned strands and replaceable hysteretic damping devices. Different arrangements of replaceable hysteretic devices were tested to study the seismic performance of the frame. Al-Janabi *et al.* [49] investigated the seismic performance of EBFs with self-centring conical friction dampers as seismic links. This device consists of steel plates with conical surfaces clamped by PT tendons. The energy dissipation mechanism is provided by the relative movement of the conical surfaces, while the compressive forces of the PT tendons provide the self-centring behaviour.

Although experimental and numerical results demonstrated the self-centring behaviour of these systems, the EBFs equipped with these devices still suffer from the detrimental frame expansion effect and local slab damage due to the gap-opening and closing mechanisms. To overcome this issue, Rezvan *et al.* [50] investigated a self-centring EBF with sliding rocking link beams and replaceable hysteretic dampers. In this case, the link is able to accommodate the expansion between the rocking link and the side beam, overcoming the 'beam growth' phenomenon. The self-centring capability is enabled by PT steel-stranded cables, while the energy dissipation of the system is provided by the yielding flexural mechanism of the plates.

Furthermore, other solutions for self-centring EBFs are based on the use of super-elastic SMA bolts [51,52], tendons [53] or dog-bone shaped plates [54]. However, although some studies demonstrated the feasibility of these solutions for seismic-resilient structures, their application is still limited by several factors, such as the cost of the material and of the manufacturing process.

Within this framework, this paper presents a damage-free self-centring link (SC-link) for EBFs. The seismic device employs post-tensioned high-strength steel bars (PT-bars) with disk springs to control the self-centring capacity of the frame and FDs to dissipate the seismic energy. The flag-shape behaviour and the analytical equations governing the global behaviour of the connection are provided. A four-storey EBF has been designed according to Eurocode 8 [1] with conventional short links and upgraded with the proposed SC-links. The third storey of the structure is extracted to develop refined 3-D finite element (FE) models in ABAQUS [55]. The results of the FE simulations are used to capture the local behaviour of the seismic device and validate the accuracy of the analytical predictions. Moreover, based on the 3-D FE modelling results, a simplified 2-D FE model is developed in OpenSees [56]. Non-linear static push-pull analyses have been performed, and Incremental Dynamic Analyses (IDA) are carried out considering a set of 30 ground motion records accounting for the record-to-record variability. The seismic performances of the EBFs with conventional links (EBF) and with SC-links (SC-EBF) are investigated and compared. The spectral acceleration corresponding to the fundamental period of vibration (*i.e.*, $S_a(T_1)$) is used as Intensity Measure (*IM*), while residual and peak interstorey drifts, as well as residual and peak link rotations, are used as Engineering Demand Parameters (EDPs). The results of the conventional and upgraded systems are compared, showing the influence of the SC-links on the seismic performance of the frames.

2. DAMAGE-FREE SELF-CENTRING LINK

2.1 Concept and structural details

Figure 1 shows the proposed SC-link. It consists of FDs to dissipate the seismic energy and PT-bars with disk springs able to develop restoring forces in the system providing the self-centring behaviour of the connection. The device is placed between the collector beams of an EBF, and it is connected to them through pins. The beam-link connections are located at the top and bottom flanges, where plates are welded to allow the placement of the pins. The SC-link's cross-section is composed of a T- and two L-plates placed in such a way as to reproduce an I-shaped profile. Symmetrical FDs are realised by slotting the web of the T-plate and adding friction pads of thermally sprayed steel shims, pre-stressed with high-strength bolts at the interface of T- and L-plates (Figure 1(b)). The slotted holes are designed to accommodate the design target rotation (*i.e.*, link rotation angle, θ_{PR} equal to *0.08 rad* in the present study according to the maximum seismic demand assumed by Eurocode 8 for short links [1]). PT-bars are placed symmetrically and post-tensioned against anchor plates outside the section of the SC-link. The PT-bars post-tensioning force acts at both ends of the SC-link, ensuring the firm contact between the anchor plates and the T- and L-plates sides and, thus, the transmission of the restoring forces. Besides, disk springs are installed to ensure the elastic behaviour of the PT-bars during their elongation (Figure 1(b)). Disk springs (or Belleville springs, [57]-[58]) are conical washer-type springs which can be arranged in parallel and in series, allowing an adequate stiffness-resistance balance to the self-centring system (Figure 1(c)). Additionally, doubler plates are welded to the collector beams' web to increase its strength and stiffness, as indicated in Figure 1(d). It is worth mentioning that the flooring system of the SC-EBFs is based on a disconnected steel-concrete slab in order to avoid damage due to the link rotation. Similar solutions have been used in previous studies [*e.g.*, 59].

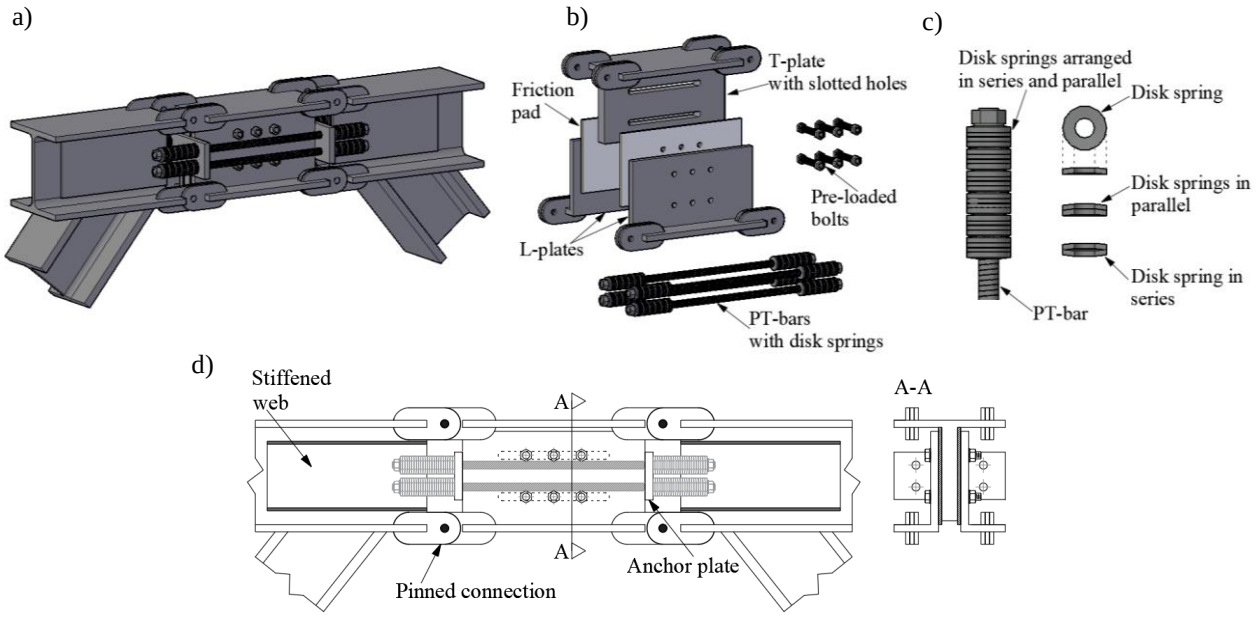

Figure 1. Damage-free self-centring link: (a) 3-D view; (b) details of the friction devices (FDs) and self-centring system; (c) details of PT-bars and disk springs; (d) lateral view and section.

2.2 Analytical model and hysteretic behaviour

According to Kasai *et al.* [60], the bending moments in columns of EBFs under the design target rotation can be assumed as negligible. Hence, analytical formulations describing the frame's force-displacement (or moment-rotation) response can be defined considering an EBF sub-assembly hinged at the base. With this simplification, Figure 2(a) and (b) schematically show the deformed shape of a generic EBF sub-assembly and the free-body diagram of the forces acting on it, respectively. In addition, the corresponding rotational equilibrium of the isolated SC-link is reported in Figure 2(b). The forces acting on the SC-link are longitudinal shear forces acting along the *x*-direction and transverse shear forces acting along the *z*-direction.

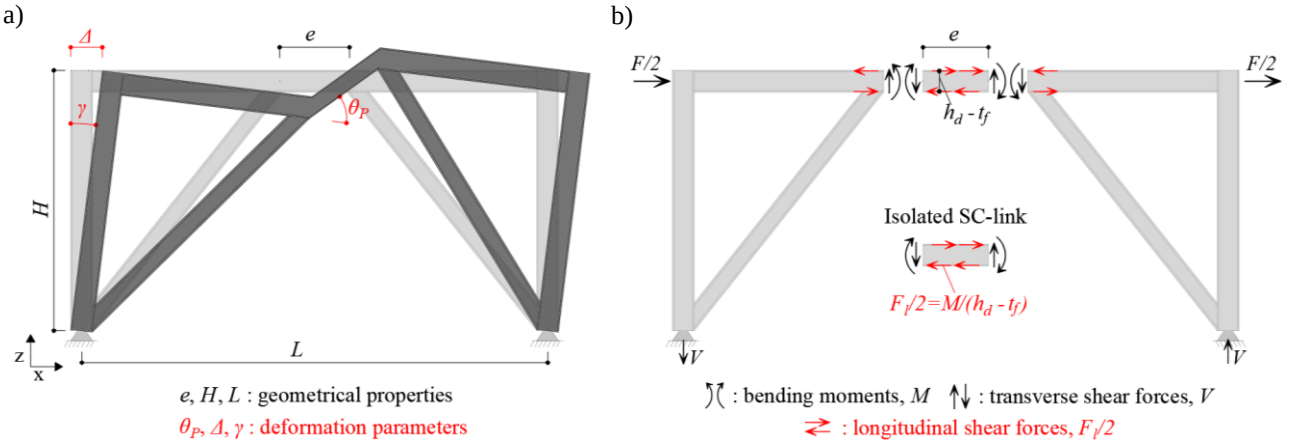

Figure 2. (a) Deformed shape of the EBF sub-assembly; (b) Free-body diagram of the forces acting on EBF sub-assembly and isolated SC-link.

The SC-link is subjected to a constant transverse shear force and double-curvature bending along its length. The transverse shear force (V), the bending moments (M) and the longitudinal shear force (F_l) acting in the SC-link are given by:

$$V = \frac{FH}{L}; \qquad M = V\frac{e}{2}; \qquad F_l = 2\frac{M}{h_d - t_f} = \frac{FHe}{L(h_d - t_f)}; \tag{1}$$

where H is the storey height; L is the span length; F is the storey's shear force; e is the link's length; t_f and h_d are the flange thickness and the section height of the link, respectively. Figure 3(a) and (b) show the kinematic mechanism of the SC-link, including the expected longitudinal shear forces developed during its rotation, and the flag-shape cyclic relationship of the SC-link, respectively. As illustrated in Figure 3(a), the link's rotation generates the gap-opening mechanism of the connection and the longitudinal sliding between the T- and L-plates (*i.e.*, within the FD), inducing the elongation of the PT-bars. Consequently, the increase of the tension forces in the PT-bars, along with the compression of the disk springs, provides the restoring forces to the SC-link. The restoring forces are transmitted to the SC-link through the anchor plates, which remain in contact with the T- and the L-plates corners during the longitudinal sliding. The deformation parameters describing the SC-link's behaviour are related to the geometrical properties of the frames (Figure 2(a)) and can be determined as follows:

$$\theta_P \cong \gamma\frac{L}{e} = \frac{\Delta}{H}\frac{L}{e}; \qquad \delta_l \cong \theta_P(h_d - t_f); \tag{2}$$

where θ_P represents the rotation between the link and the beam; γ represents the drift ratio; Δ is the frame sway displacement; δ_l is the longitudinal sliding which provides the damping mechanism of the SC-link. Besides, in Figure 3(a), F_{FD} is the sliding force developed in the friction pads; $F_{PT,0}$ is the post-tensioning force in the PT-bars; ΔF_{PT} is the additional post-gap-opening force in the PT-bars. The flag-shape cyclic relationship of the SC-link (Figure 3(b)) is reported in terms of longitudinal shear force acting in the link (*i.e.*, F_l) vs. longitudinal sliding (*i.e.*, δ_l). It is worth noting that the formulations listed in Eqn. (1) can be used to represent the analytical response in terms of transverse shear force – longitudinal sliding (*i.e.*, V - δ_l), transverse shear force – link rotation (*i.e.*, $V - \theta_P$), bending moment – link rotation (*i.e.*, $M - \theta_P$) into a form equivalent to $F_l - \delta_l$ relationship. The backbone flag-shape curve of the device consists of four branches: the first and the second branches represent the loading phase before and after the gap-opening mechanism occurs (due to the longitudinal sliding in the SC-link), respectively, up to the maximum longitudinal sliding $\delta_{l,d}$ (the corresponding link rotation can be derived by applying the Eqn. (2)). The third and the fourth branches describe the unloading phase during which the SC-link returns to its initial position. The stiffnesses of the branches are equal to the stiffness of the first (*i.e.*, k_1) and the second branch (*i.e.*, k_2), respectively. The first one (*i.e.*, k_1) is characterised by an infinite stiffness value due to the rigid behaviour of the connection before the gap-opening mechanism occurs. The stiffness of the second branch (*i.e.*, k_2) depends on the stiffness of the system PT-bars and disk springs.

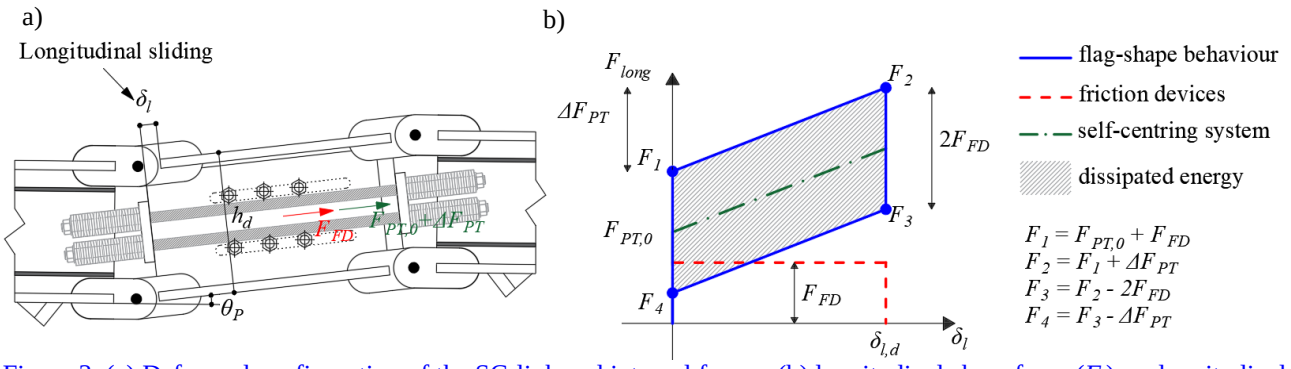

Figure 3. (a) Deformed configuration of the SC-link and internal forces; (b) longitudinal shear force (F_l) vs. longitudinal sliding (δ_l).

The longitudinal shear forces' contributions defining the entire cycle (*i.e.*, F_1, F_2, F_3, and F_4), are shown in Figure 3(b). Besides, the F_2/F_1 ratio represents a measure of the strain-hardening developed within the SC-link at $\delta_{l,d}$. The main parameters which allow deriving each significant point are F_1 and ΔF_{PT}. F_1 is the sum of the initial post-tensioning force applied in the PT-bars (*i.e.*, $F_{PT,0}$) and the sliding forces developed in the friction pads (*i.e.*, F_{FD}). In the analytical model, the FDs are characterised by a rigid-plastic hysteretic behaviour, which depends on the clamping force and the friction coefficient μ of the contact interfaces. According to Coulomb's friction law, the friction forces are given by:

$$F_{FD} = \mu n_s n_b F_{preload,FD} \tag{3}$$

where μ is the friction coefficient of the interfaces; n_s is the number of the friction interfaces (*i.e.*, two in the considered configuration); n_b is the number of bolts in the FDs; $F_{pre\text{-}load,FD}$ is the pre-loading force of each bolt. The increase of force in the PT-bars due to elongation (ΔF_{PT}) is a function of the stiffness of the system of PT-bars and disk springs [57-58] and is given by:

$$\Delta F_{PT} = K_{eq}\delta_l; \qquad K_{eq} = \frac{K_{PT}K_{ds}}{K_{PT}+K_{ds}}; \qquad K_{PT} = \frac{n_{PT}E_{PT}A_{PT}}{l_{PT}}; \qquad K_{ds} = \frac{n_{ds,par}}{n_{ds,ser}}K_{ds,1}; \tag{4}$$

where K_{eq} represents the equivalent axial stiffness of the self-centring system; K_{PT} and K_{ds} represent the stiffness of the PT-bars and the disk spring, respectively; n_{PT} is the number of PT-bars in the SC-link; E_{PT}, A_{PT}, l_{PT} are, respectively, the Young's modulus, the cross-sectional area and the length of each PT-bar; $n_{ds,par}$ and $n_{ds,ser}$ are the number of disk spring in parallel and in series, respectively. Considering the flag-shape behaviour and the equations to derive it, it is easy to recognise that, from a design point of view, the self-centring behaviour is achieved if the following inequality is satisfied:

$$F_4 \geq 0 \rightarrow F_{PT,0} \geq F_{FD} \tag{5}$$

2.3 Design procedure

The design of the SC-link is based on the structural analysis of the equivalent conventional EBF system at the design limit state (*i.e.*, Ultimate Limit State – ULS). According to the analytical model presented in the previous section, the design transverse shear force and design longitudinal shear force are derived from Eqn. (1), considering F as the lateral equivalent force to the seismic design action. Furthermore, the design longitudinal sliding (*i.e.*, $\delta_{l,d}$) is derived from Eqn. (2) considering θ_P as the design link rotation.

The T-plate, L-plates, anchor plates, and pin connections should be designed to remain elastic. Hence, their resistance must be verified against their maximum forces at the design link rotation. In particular, F_2 (Figure 3) represents the maximum longitudinal shear force acting in the SC-link. Considering this value, Eqn. (1) provides the maximum transverse shear force (*i.e.*, V_2) and the maximum value of the bending moment (*i.e.*, M_2).

Based on the cross-section of the collector beams, the dimensions of the links' cross-section are selected according to practical and geometric considerations. For the sake of simplicity, the link height (h_d) is taken equal to the height of the collector beams. This allows simplifying the geometry and manufacturing of the device. The other geometrical properties of the T- and L-plates (thickness of the webs and flanges) are designed to prevent their damage and, thus checked against the aforementioned maximum forces, considering both shear and bending resistance. Furthermore, to allow the gap-opening mechanism of the SC-link, the T-plate's holes are designed to accommodate $\delta_{l,d}$. At the same time, the slotted section must be verified against F_2, considering the bearing resistance. The pin connections are designed to transmit the transverse shear forces and bending moments through their equivalent horizontal force components. They are designed according to Eurocode 3 requirements [61] and verified for V_2 and M_2. Specifically, each pin is designed with $V_2/4$ and

(M_2/(h_d-t_f))/2 as design actions and considering their failure modes (*i.e.*, shear resistance of the pin, bearing resistance of the plate and the pin, bending resistance of the pin, combined shear and bending resistance of the pin, as indicated in [61]).

The self-centring capability is provided by distributing the design longitudinal shear force (F_l) between the FDs and the self-centring system, according to Eqn. (5). In particular, $\gamma_{SC}F_l$ and $(1 - \gamma_{SC})F_l$ represent the design forces of the self-centring system and FDs, respectively. γ_{SC} is the repartition factor of F_l, which needs to be greater than 0.5 to ensure the self-centring capability of the system. The design longitudinal shear force of the self-centring system ($\gamma_{SC}F_l$) is the initial post-tensioning force of the PT-bars (*i.e.*, $F_{PT,0}$) and allows designing the number and dimension of the PT-bars. Successively, the number of disk springs in parallel and in series is calculated. The number of disk springs in parallel (*i.e.*, $n_{ds,par}$) is determined based on the bar's yielding resistance. Conversely, the number of disk springs in series (*i.e.*, $n_{ds,ser}$) depends on the equivalent axial stiffness of the self-centring system and must provide sufficient deformability to the SC-system to avoid the PT-bars' plasticisation at $\delta_{l,d}$. The parameters $n_{ds,par}$ and $n_{ds,ser}$ can be calculated as follow:

$$n_{ds,par} \geq \frac{N_{y,PT}}{F_{ds,1}}; \qquad \frac{N_{y,PT} - N_{PT,0}}{\delta_{l,d}} = K_{eq,1} \geq K_{eq} \rightarrow n_{ds,ser} \geq n_{ds,par} K_{ds,1} \left(\frac{K_{PT} - K_{eq,1}}{K_{eq,1} K_{PT}} \right) \tag{6}$$

where $N_{y,PT}$ is the yield strength of the PT-bar; $F_{ds,1}$ is the resistance capacity of a single disk spring; $N_{PT,0}$ is the post-tensioning force of the PT-bar. It is noteworthy that Eqn. (6) provides the minimum number of $n_{ds,ser}$. This value can be further increased to reduce K_{eq} and, consequently, decrease the maximum longitudinal shear forces (F_2) used to design the geometrical properties of the SC-link (*i.e.*, T- and L-plates, pin connections).

Successively, the anchor plates for the PT-bars are designed. The height and width of the anchor plates are defined according to geometric considerations, while the thickness is designed to resist the total force of the PT-bars (*i.e.*, $F_{PT,0} + \Delta F_{PT}$) and to have sufficient stiffness, guaranteeing the fully transmission of the restoring forces to the SC-link.

In conclusion, the FDs are designed such that the slippage force (F_{FD}) on the FD interfaces resists the remaining design longitudinal shear force (*i.e.*, $F_{FD} = (1 - \gamma_{SC})F_l$). The number of bolts can be designed based on the Eqn. (3), by choosing the diameter and the class of the bolts, and ensuring that the pre-loading force in each bolt ($F_{pre\text{-}load,FD}$) is smaller than the maximum pre-loading force (*i.e.*, $F_{p,Cd}$) defined in [61].

3. CASE-STUDY STRUCTURE

3.1 Design of the eccentrically braced frame

Figure 4 shows the plan and elevation views of the four-storey, five-bay by three-bay prototype steel residential building selected for case-study purposes. The layout has interstorey heights of 3.20 m except for the first level, which is equal to 3.50 m, while all bays have a span length of 6 m. Seismic-resistant perimeter K-type EBFs are located in the *x*-direction, while the interior part is composed of gravity frames (*i.e.*, pinned beam-to-column connections and column bases). Composite deck slab floors are employed, producing a rigid horizontal diaphragm, providing stability to the overall building system.

The study focuses on the assessment of the EBFs in the *x*-direction. Two configurations are analysed and compared: the conventional EBF and the equivalent SC-EBF. The conventional EBF has been designed according to the Eurocode 8 recommendations and successively upgraded with the proposed SC-links.

Steel S275 is used for all structural elements (*i.e.*, columns, beams, and braces). The gravity and variable loads are assumed to be uniformly distributed with values of G_k = 4.5 kN/m^2 and q_k = 2 kN/m^2 (*i.e.*, suggested values for residential buildings), while the cladding load is assumed as 2.0 kN/m. The seismic mass, according to the Eurocode 8 [1] seismic combination, is equal to 156.1 and 154.4 tons, respectively, for the intermediate storeys and the roof. The cross-section profiles for the gravity columns are HE 200B at the first and second storey, while HE 180B are adopted for the third and fourth storey. The design earthquake at the ULS (probability of exceedance of 10% in 50 years) is defined considering a Type-1 elastic response spectrum with a peak ground acceleration equal to 0.35 g and soil type C [1]. The seismic action at the Collapse Limit State (*i.e.*, CLS, probability of exceedance of 2% in 50 years) is assumed to have an intensity equal to 150% of the ULS. The behaviour factor (q) is assumed equal to 6.0 according to Eurocode 8 [1] for EBFs designed in Ductility Class High (DCH). The length e of the links is limited at an upper value of 1.6 $M_{p,link}/V_{p,link}$ according to the provisions for short links. In addition, to achieve a global dissipative behaviour of the structure, the link overstrength (*i.e.*, Ω defined as 1.5 $V_{p,link}/V_{Ed,i}$ for short links according to [1]) at each storey do not exceed the minimum Ω by more than 25% [1]. The design results are summarised in Table 1, while the Ω distribution is reported in Figure 5(a). Additionally, to ensure an adequate link rotation capacity, intermediate web stiffeners spaced at an interval not exceeding $(30t_w - d/5)$ are included, according to requirements for short links [1]. Doubler and continuity plates are used to ensure sufficient

strength and stiffness to beam-to-column joints. Figure 5(b) shows the distribution of the interstorey drifts evaluated for the serviceability check at the Damage Limit State (*i.e.*, DLS, probability of exceedance of 10% in 10 years). It is important to highlight that, for the considered EBF, the requirements at the ULS control the design while the serviceability limitations are largely satisfied. In fact, the interstorey drifts shown in Figure 5(b), are much smaller than the interstorey drift limit (assumed as 1%, accordingly to Eurocode 8 [1]). Finally, the *P-Δ* effects are not taken into account since the interstorey drift sensitivity coefficient (calculated following the Eurocode requirements [1]) is less than 0.1 at all the storeys. Figure 6 shows the hysteretic responses of the conventional link of the EBF in terms of link transverse shear (V) vs. link rotation (θ_P).

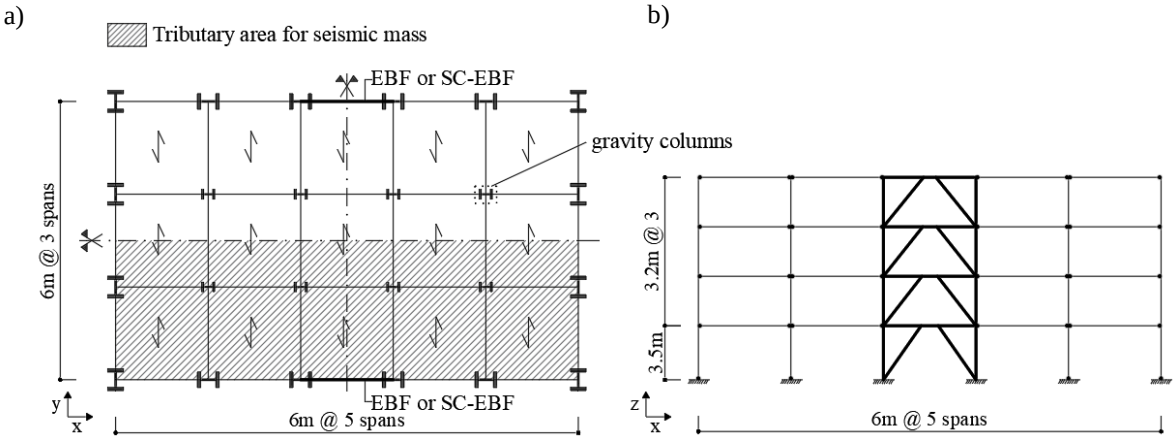

Figure 4. (a) Plan view and (b) Elevation view of the case-study building with EBF.

Table 1. Design results or the EBF.

Storey	Brace section	Column section	Link section	Link length, e [mm]
1st	HE 240M	HE 320B	HE 360B	1100
2nd	HE 220M	HE 320B	HE 320B	1000
3rd	HE 200M	HE 280B	HE 280B	900
4th	HE 180M	HE 280B	HE 200B	600

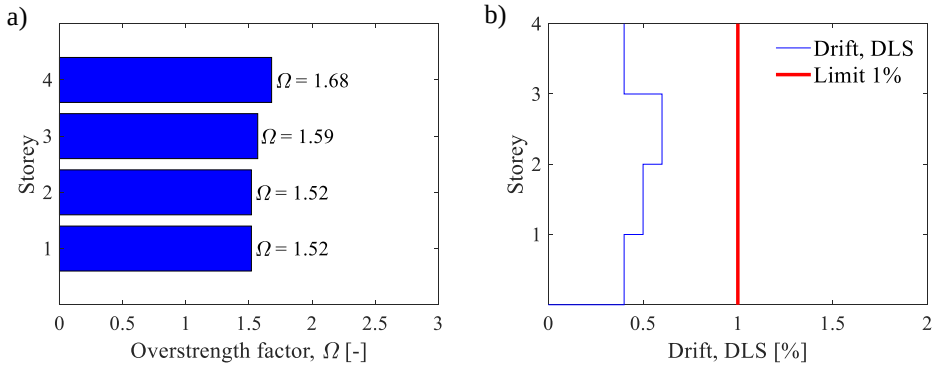

Figure 5. (a) Link overstrength (Ω, [1]) distribution; (b) Drift distribution for the serviceability check at DLS.

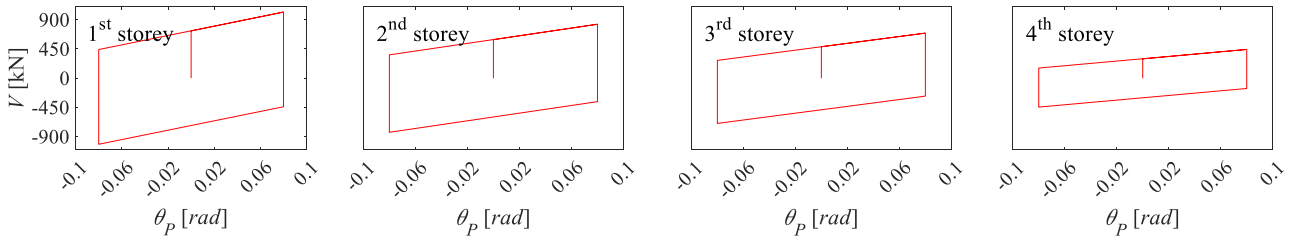

Figure 6. Hysteretic response of conventional links in terms of link transverse shear (V) vs. link rotation (θ_P) for the EBF.

3.1 Design of the damage-free self-centring links (SC-links)

The EBF has been upgraded with the SC-links herein proposed. The SC-links have been designed based on the ULS limit state, according to the procedure presented in Section 2.3. In particular, the design action of each SC-link is provided by Eqn. (1), in which F represents the total storey shear demand of the EBF. According to Eqn. (5), by adopting a repartition factor (γ_{SC}) equal to 0.6, the design actions are equal to $0.6F_{l,d}$ and $0.4F_{l,d}$ for the self-centring system and FDs, respectively. Table 2 reports the design longitudinal shear forces of the SC-links and the corresponding values to define their components. In addition, assuming a design link rotation equal to $\theta_{PR} = 0.08\ rad$, the design longitudinal sliding ($\delta_{l,d}$) of the SC-links is provided by the Eqn. (2) and indicated in Table 2. Besides, the F_2/F_1 ratio is limited to 1.5, consistently to the minimum Ω value defined in the Eurocode 8 [1] for short links.

The friction pads are chosen according to the tests carried out by Cavallaro *et al.* [62] and consist of 8 mm thick thermally sprayed friction metal steel shims with a friction coefficient $\mu = 0.53$. HV bolts of 10.9 class have been selected for the FDs, and high-strength bars of 10.9 class have been used for the self-centring systems. The number and the pre-load for the bolts of the FDs and PT-bars of the SC-links are summarised in Table 3. Finally, based on Eqn. (6) disk springs are arranged in series and parallel, providing the equivalent stiffnesses to the self-centring systems reported in Table 3. The hysteretic behaviour of the SC-links, obtained by applying the formulations presented in Section 2.2, is illustrated in Figure 7 in terms of link transverse shear (V) vs. link rotation (θ_P). The EBF and SC-EBF are characterised by the same fundamental period of vibration $T_1 = 0.55$ sec. The corresponding spectral accelerations at the ULS ($S_a(T_1)_{ULS}$) and the CLS ($S_a(T_1)_{CLS}$) are 1.2g and 1.8g, respectively.

Table 2. Longitudinal shear forces and sliding of SC-links' components of the SC-EBF.

Storey	Total longitudinal shear force, F_l [kN]	Longitudinal shear force of the FDs, $(1 - \gamma_{SC})F_l$ [kN]	Longitudinal shear force of the SC-system, $\gamma_{SC}F_l$ [kN]	Longitudinal sliding, $\delta_{l,d}$ [mm]
1st	2152	861	1291	29
2nd	1802	721	1081	26
3rd	1434	574	860	23
4th	768	307	461	16

Table 3. Design results of SC-links for the SC-EBF.

Storey	Bolts [-]	Bolt pre-load [kN]	PT-bars [-]	PT-bar post-tension [kN]	K_{eq} SC-link [N/mm]
1st	6 M22	135	4 M30	323	6899
2nd	6 M20	113	4 M27	270	5490
3rd	6 M18	90	4 M24	215	4434
4th	4 M16	72	4 M20	115	5992

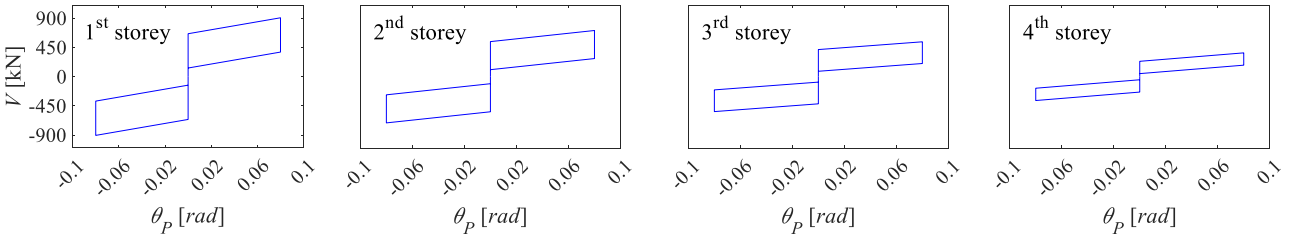

Figure 7. Hysteretic response of SC-links in terms of link transverse shear (V) vs. link rotation (θ_P) for the SC-EBF.

4. NUMERICAL MODELS AND CYCLIC RESPONSE OF THE DAMAGE-FREE SELF-CENTRING LINK

4.1 SC-link properties

The third storey of the case-study structure presented in the previous section is extracted to investigate the behaviour of a sub-assembly upgraded with the proposed SC-link and the local response of the device. The cyclic behaviour of such sub-assembly has been assessed considering both the EBF and the SC-EBF. The geometry of the investigated SC-link is illustrated in Figure 8. The SC-link depth is equal to 280 mm, and it is composed of T- and L-plates whose geometrical

properties are summarised in Table 4. FDs are realised with S275 steel plates, characterised by a thickness of 8 mm and thermally sprayed with frictional metal shims with a friction coefficient μ = 0.53 [62]. Besides, steel S355 is adopted for the PT-bars' anchor plates and pins' connection plates. The anchor plates for the PT-bars have dimensions equal to 140 × 280 × 50 mm (*i.e.*, height, width and thickness, respectively), as shown in Figure 8. Pins with a diameter equal to 20 mm and four connection plates are used for each pin connection. Four HV M24 10.9 class PT-bars with a length of 1.9 m each are employed in the SC-system. Standard disk springs with a diameter equal to 56 mm, thickness equal to 6 mm and height equal to 6.8 mm are used. The resistance and stiffness of each disk spring are, respectively 122 kN and 87739 N/mm. The disk springs' arrangement provides K_{eq} equal to 4434 N/mm, as previously reported in Table 3. Doubler plates of 10 mm have been included to increase the strength and stiffness of the collector beams.

Table 4. Properties of the SC-link for the third story.

	H [mm]	t_w [mm]	t_f [mm]	b [mm]	L [mm]	Steel grade
T-plate	252	40	18	280	810	S275
L-plates	252	20	18	280	810	S275
FDs shims	244	8	-	-	810	S275 – thermally sprayed

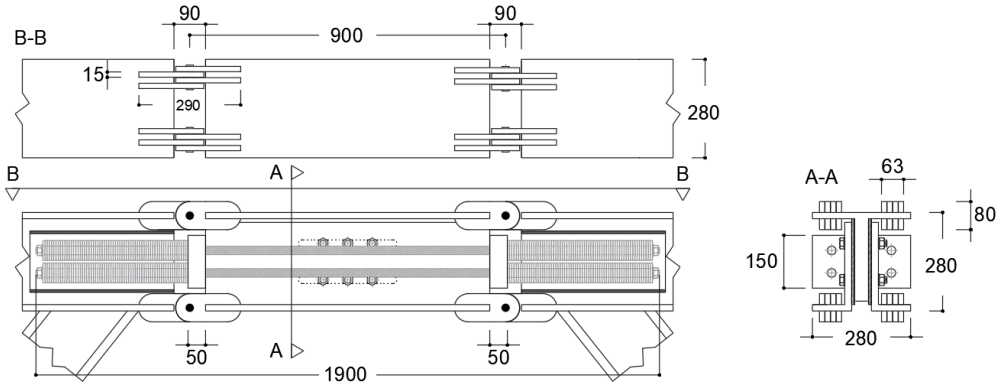

Figure 8. Geometry of the SC-link for the third story (dimensions in mm).

A detailed 3-D FE model in ABAQUS [55] and a simplified 2-D FE model in OpenSees [56] of the sub-assembly of the third story are developed and presented in the following sections to simulate their cyclic behaviour. The 3-D FE model is used to capture the local behaviour of the components and validate the analytical formulation describing the behaviour of the device. The 2-D FE model in OpenSees is validated against the results of the 3-D FE ABAQUS model and successively used in Section 5 to perform non-linear time-history analyses of the entire SC-EBF to evaluate its global response.

4.2 Finite Element (FE) model in ABAQUS

3-D FE models of the third story of the case-study frames in both configurations (*i.e.*, EBF and SC-EBF) are developed in ABAQUS [55]. The typical mesh and details of the models are shown in Figure 9. The eight-node linear brick element (C3D8R) are used in the modelling. The EBF and SC-EBF are pinned at the base (according to the assumptions made in Section 2.2). The models are constituted by *'wire'* elements for columns and the portions of braces and beams away from the link. 3-D solid elements are adopted for the other parts (*i.e.*, link section, portions of braces and beams close to the link, bolts, PT-bars and anchored plates). A '*tie constraint*' is used to simulate welding among stiffener and beam, bracing and beam, column and beam. The *'surface-to-surface'* interaction property is used to define the contact behaviour among friction interfaces of the FDs and steel parts. In particular, the *'Hard Contact'* option is adopted to describe the behaviour of the interaction in the normal direction, whereas the tangential behaviour is modelled by adopting a *'Penalty'* friction formulation with friction coefficients equal to 0.30 for interfaces among steel parts and 0.53 for FDs [62]. In addition, the relative motion is defined using the finite-sliding approach. It is noteworthy that no constraints are applied to attach the anchor plates, and the aforementioned interaction property is used to describe the contact behaviour between the anchor plates and the T- and L-plates corners (with friction coefficient of 0.30). The *'bolt load'* is used to model the pre-loading in the bolts and the *'apply force'* option is used to keep the force constant during the analysis. The self-centring system is modelled only by including the PT-bars. The disk springs are not explicitly included in the model, and their contribution is taken into account by assigning to the PT-bars an equivalent axial stiffness (*i.e.*, K_{eq}). The post-tensioning in the PT-bars is modelled as a thermal field applying a *'predefined field temperature'* and calibrating its magnitude to have the $F_{PT,0}$ design value in each PT-bar. The materials' mechanical properties are defined according to an elastic-plastic

behaviour. In particular, Young's modulus and Poisson ratio equal to 210 GPa and 0.3 are adopted for the elastic behaviour, respectively, while the plasticity is described with '*isotropic hardening*'.

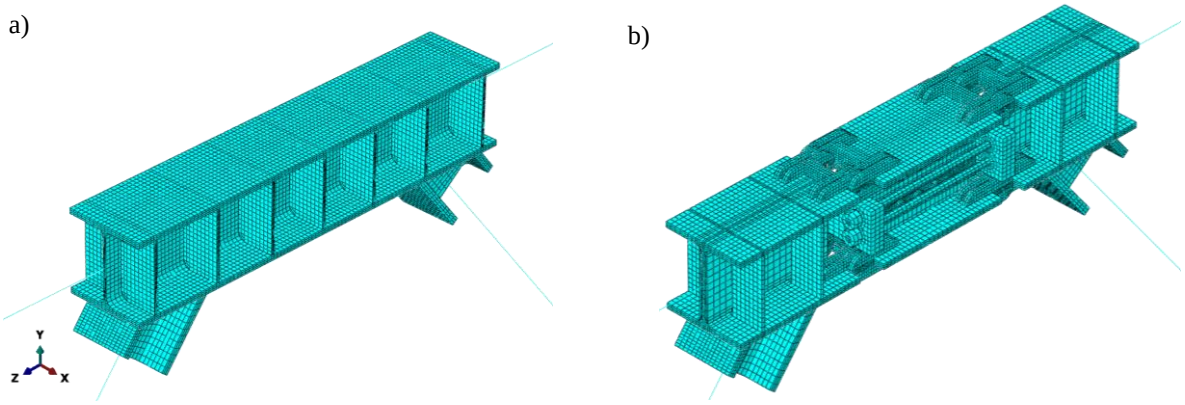

Figure 9. ABAQUS [55] modelling: 3-D views of (a) conventional link; (b) SC-link.

4.3 Finite Element (FE) model in OpenSees

2-D FE models of the EBF systems in both configurations (*i.e.*, EBF and SC-EBF) are developed in OpenSees [56]. To accurately consider the interaction between bending moments and axial forces, columns, beams and bracings are modelled using fibre section '*nonlinearBeamColumn*' elements with four integration points. Additionally, the '*section Aggregator*' function is used to model the plastic shear capacity (*i.e.*, $V_{pl,Rd}$ as defined in [1]) of columns, beams and bracings. The '*Steel01*' material with 275 MPa yield strength and 0.2% post-yield stiffness ratio is employed for columns, bracings and beams. At beam-to-column connections, elastic elements with very high flexural stiffness are used to simulate their full-strength rigid behaviour. The seismic links are modelled with two '*nonlinearBeamColumn*' connected in their mid-section through a non-linear vertical spring modelled as a '*zeroLength*' element. This modelling strategy is used for both configurations (*i.e.*, EBF and SC-EBF). Conversely, the material assigned to the zero-length element is different between the two models: the '*Steel 01*' material is adopted for conventional EBF, whereas the '*SelfCentering*' material is used to model the SC-link in the SC-EBF. A very high initial stiffness is assigned to the material models for both links to account, in one case for the shear stiffness of the conventional link and, in the other case, for the rigid-plastic behaviour of the device. For the conventional link, the yield strength is equal to the plastic shear of the link (*i.e.*, $V_{p,link}$ defined in [1]) increased by 15%, taking into account the kinematic hardening effect not explicitly modelled in OpenSees [56]. A strain-hardening ratio of 0.003 is used. For the SC-link, the post-gap-opening stiffness is assigned equal to k_2, whereas $2F_{FD}$ defines the amplitude (*i.e.*, the energy dissipation provided by the FDs) of the SC-link flag-shape behaviour.

4.4 Comparison of the numerical results

The results of the ABAQUS [55], OpenSees [56] and the previously described analytical model are compared. Cyclic simulations have been performed for the two models, considering the same lateral displacement history. In particular, horizontal displacements are applied along *z*-direction (Figure 9), with an increasing amplitude at each step up to a maximum displacement of 32 mm, corresponding to a link rotation of about 0.07 *rad*. The cyclic behaviour in terms of lateral force (F) vs. lateral displacement (Δ) of the frame is illustrated in Figure 10(a) and Figure 10(c) for the EBF and the SC-EBF, respectively. Similarly, the cyclic behaviour in terms of link transverse shear (V) vs. link rotation (θ_P) is illustrated in Figure 10(b) and Figure 10(d) for the EBF and the SC-EBF, respectively. The hysteretic curves of the EBF have a stable cyclic behaviour characterised by cyclic hardening without degradation of the stiffness. Conversely, the results of the SC-EBF show that the connection proposed is able to provide the self-centring capability to the system. The results show a good agreement among the ABAQUS [55] and OpenSees [56] models. For large displacement, the ABAQUS model of the sub-assembly with SC-link (Figure 10(c) and (d)) shows a slight increase of the force predicted. This is due to the axial restraint provided by the pin connections for large rotations of the SC-link, with a consequent occurrence of tensile axial forces due to second-order effects [63, 64]. This phenomenon is not captured in the 2-D modelling. In addition, by comparing the analytical flag-shape behaviour of the SC-link and the numerical hysteretic curves (Figure 10(d)), it is possible to observe that the analytical formulas presented in Section 2.2 accurately predict the hysteretic response of the SC-link.

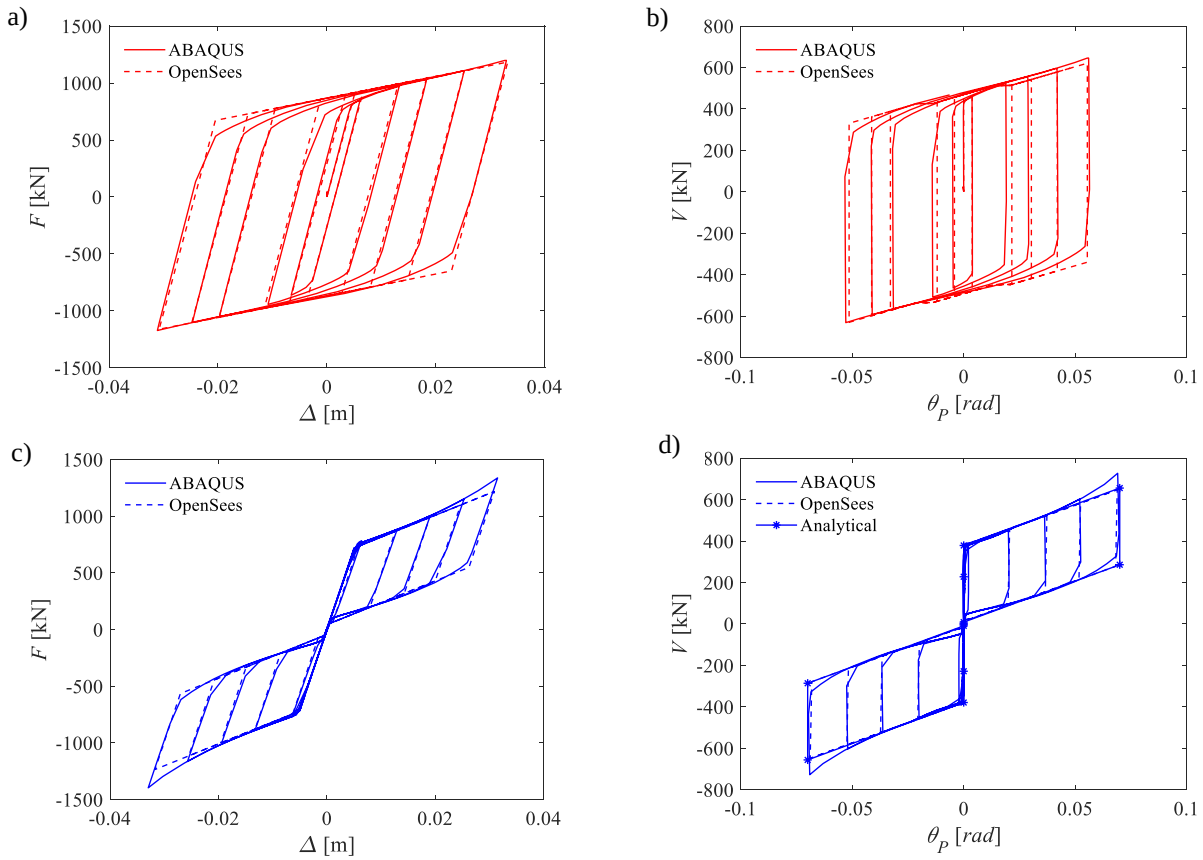

Figure 10: Comparison of the cyclic behaviour in terms of lateral force (F) vs. lateral displacement (Δ) of the frame for (a) EBF and (c) SC-EBF; and in terms of link transverse shear (V) vs. link rotation (θ_P) for (b) EBF and (d) SC-EBF.

Figure 11(a) and (b) show the Von Mises stress distributions obtained from the ABAQUS results, corresponding to a lateral displacement of 32 mm (*i.e.*, link rotation of 0.07 *rad*) of the sub-assembly in the frames with the conventional and SC-link, respectively. It can be observed that, as expected, the conventional link is subjected to extensive shear yielding (Figure 11(a)), resulting in large residual displacement (Figure 10(a)). Conversely, all regions of the SC-link are characterised by stresses lower than yielding, with only some stress concentrations in the pin connections. Additionally, the stresses observed at the T- and L-plates edges (ranging from about 130 MPa to 180 MPa) are due to the contact pressure produced by the additional axial forces developed in the PT-bars during their elongation. Furthermore, Figure 12(a) and (b) show the plastic strains (output parameter PEEQ [55]) obtained from the ABAQUS results at the end of the cyclic simulation of the sub-assembly in both configurations. As expected, significant plastic deformations are observed for the conventional link in the web panel and in the flanges adjacent to the collector beams (Figure 12(a)). Conversely, Figure 12(b) shows that the introduction of the SC-link significantly reduces the plastic deformations. In fact, no residual deformations are observed in the elements of the SC-link (*i.e.*, T- and L-plates, anchor plates). This validates the approach presented in the design procedure (Section 2.3) to avoid their yielding, hence confirming the low-yielding behaviour of the device. Some slight stress concentration and residual deformation (< 0.01 PEEQ) are observed at the collector beams' flanges adjacent to the pin connections, due to the additional tension axial forces developed in the SC-link (previously shown in Figure 10(c) and (d)) for large rotations. To mitigate this phenomenon, the thickness and the length of the plates could be slightly increased, hence increasing the transmission area of the stresses and avoiding damage.

Figure 13(a) shows the PT-bars force (F_{PT}) vs. the link rotation (θ_P) of the SC-EBF for both the ABAQUS [55] model and the analytical prediction showing a good agreement of the results. In addition, Figure 13(b) shows the ABAQUS [55] results of the bending moment (M) at different sections of the SC-link vs. the link rotation (θ_P) of the SC-EBF. In particular, M is reported for the external sections of the SC-link (right section, M - right, and left section, M - left) and at mid-length (M - mid length). These results verify the simplifying assumption presented in Section 2.2 used to define the analytical formulations.

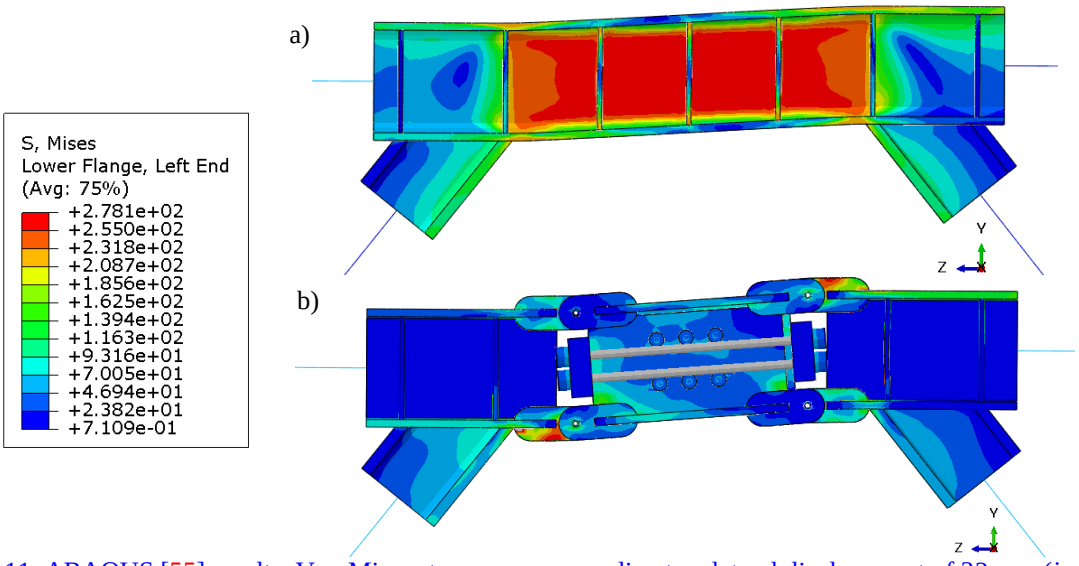

Figure 11. ABAQUS [55] results: Von Mises stresses corresponding to a lateral displacement of 32 mm (*i.e.*, link rotation of 0.07 *rad*) for (a) EBF with the conventional link and (b) EBF with SC-link.

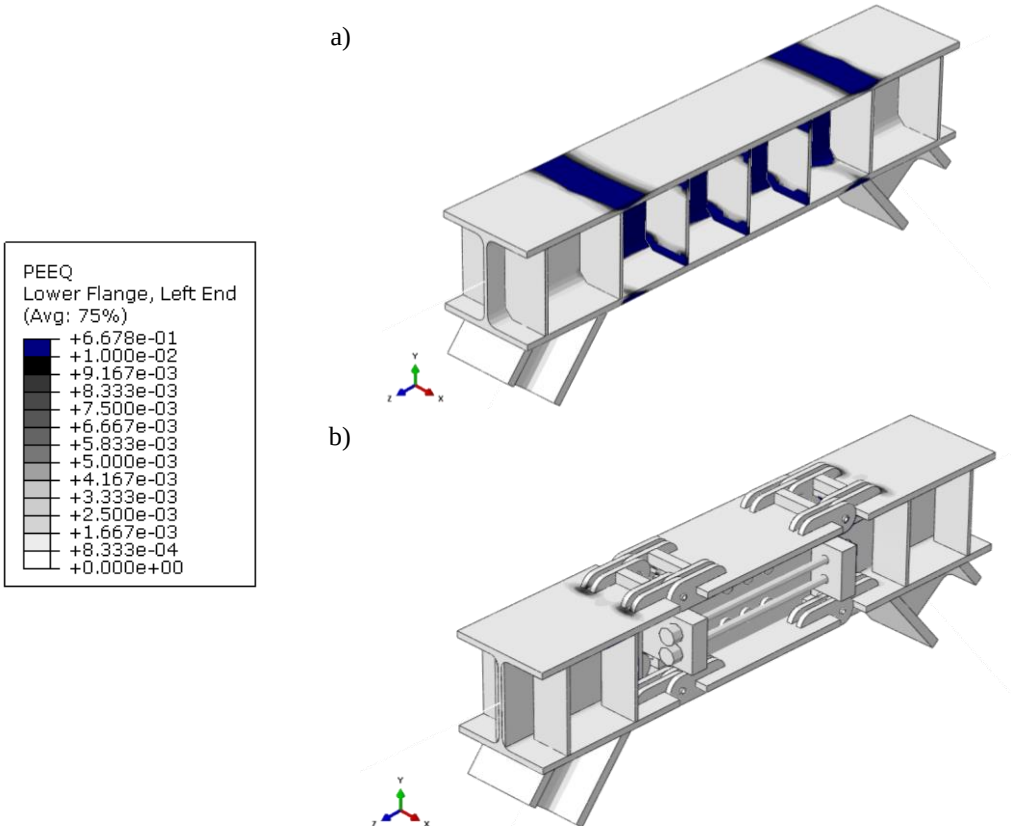

Figure 12. ABAQUS [55] results: Equivalent plastic strain (PEEQ) at the end of the cyclic simulations for (a) EBF with the conventional link and (b) EBF with SC-link.

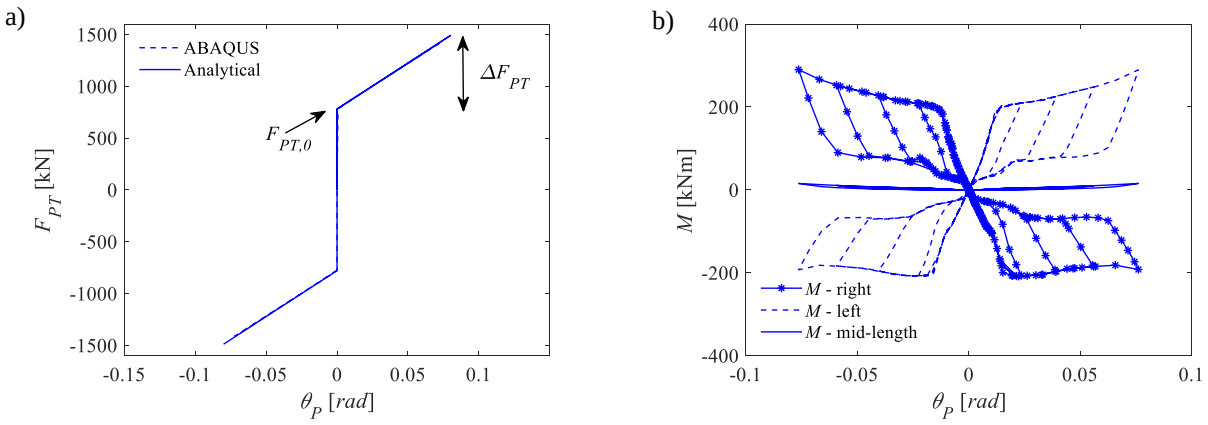

Figure 13. ABAQUS [55] results: (a) PT-bars force (F_{PT}) vs. link rotation (θ_P) and (b) bending moment (M) vs. link rotation (θ_P) within the SC-link for the SC-EBF.

5. SEISMIC RESPONSE OF THE SC-EBF

5.1 Finite Element (FE) models of the case-study EBFs

2-D FE models are developed in OpenSees [56] for the one-bay, four-storey perimeter EBF and SC-EBF in the *x*-direction. The modelling approach used for all the members (*i.e.*, beams, columns and bracings) and the links' (or SC-links) follows the one presented in Section 4.3, both for the EBF and SC-EBF. Furthermore, large displacement effects are simulated through the *P-Δ* formulation (*i.e.*, '*geomTransf PDelta*' [56]). Moreover, the *P-Δ* effects due to the gravity frame are included through a leaning column pinned at the base and continuous along with the height. It is connected to the frames through rigid trusses, and its flexural and axial stiffnesses are equal to the sum of the flexural and axial stiffnesses of the gravity columns contained in half of the building plan (Figure 4) [36]. Gravity loads are applied on the beams by considering the seismic combination of the Eurocode 8 [1], while the seismic masses are applied at beam-to-column intersections. In the dynamic analyses, the Newmark method with $\beta = 0.25$ and $\gamma = 0.5$ is used, and Rayleigh damping is adopted by considering a 2% viscous damping ratio to the first and second modes.

5.2 Push-pull analysis

Non-linear static push-pull analyses have been carried out for the case-study frame in both configurations (*i.e.*, EBF and SC-EBF). The analyses are performed as displacement-controlled up to a roof displacement equal to 0.20 m, corresponding to the mean value (among all ground motion), obtained from the non-linear time history analyses for a seismic intensity corresponding to the ULS. The non-linear time history analyses results are described in the following Section 5.4.

Figure 14 shows the comparison of the push-pull results in terms of total base shear (V_b) vs. roof displacement (Δ_{top}). As expected from the design, the EBF (red lines) results in large residual deformations due to yielding in shear of the links. Conversely, the results of the SC-EBF (blue lines) show a flag-shape behaviour of the system.

Figure 15 shows the push-pull results in terms of link transverse shear (V) vs. link rotation (θ_P) for all storeys. The comparison of the V–θ_P curves (Figure 15) highlights that small differences exist in the link rotation demand of the conventional link of the EBF and the SC-links of the SC-EBF. In particular, for the first storey (Figure 15(a)), the SC-EBF experience slightly smaller link rotations (*i.e.*, 0.11 vs. 0.12 *rads*), while for the third and fourth storeys, the SC-EBF experience slightly larger link rotations (*i.e.*, 0.12 vs. 0.09 *rads* at the third storey and 0.13 vs 0.11 *rads* at the fourth storey). Finally, the same maximum link rotations (*i.e.*, 0.12 *rad*) occur at the second storey. These differences are due to the slightly different post-yielding stiffness exhibited by the conventional links compared to the post-gap opening stiffness (*i.e.*, K_{eq}) in the SC-links. In the conventional links, the post-yielding stiffness is controlled through the Ω values defined in the Eurocode 8 [1] and previously reported in Figure 5(a). Conversely, in the SC-links K_{eq} depends on the self-centring system's design. In particular, as evidenced by Eqn. (4), its value is provided by the stiffness of the PT-bars and disk springs arrangement (*i.e.*, K_{TB} and K_{DS}, respectively).

It is worth mentioning that the SC-EBF is characterised by a reduced energy dissipation capacity with respect to the EBF, as shown in Figure 14 and Figure 15. This is a typical characteristic of self-centring systems due to their flag-shape behaviour [20], and the effects on the seismic response of the frame are discussed in the following section.

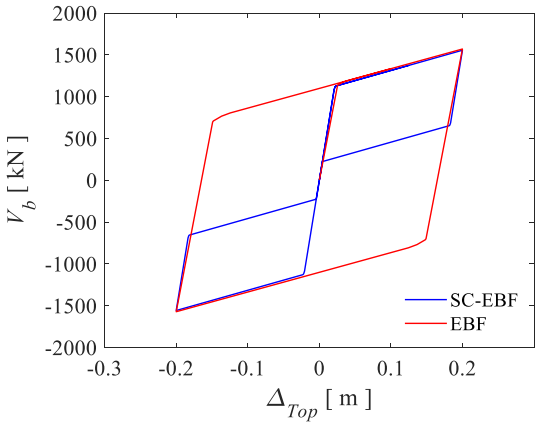

Figure 14. OpenSees [56] results: Push-pull results in terms of total base shear (V_b) vs. roof displacement (Δ_{top}) for EBF and SC-EBF.

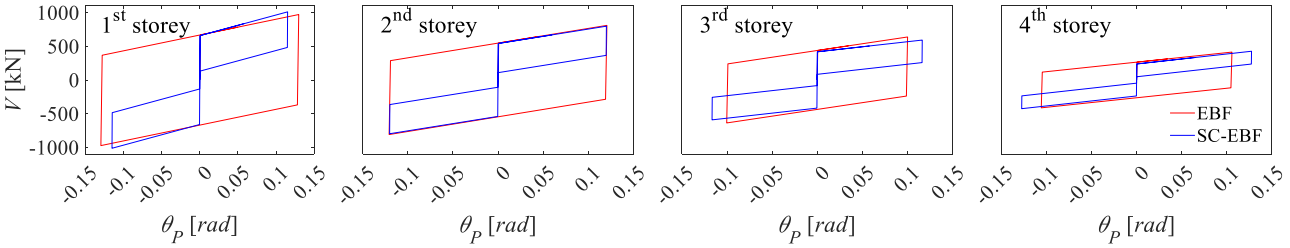

Figure 15. OpenSees [56] results: Push-pull results in terms of link transverse shear (V) vs. link rotation (θ_P) for EBF and SC-EBF.

5.3 Ground motion selection and scaling to perform time history analyses

A set of 30 natural ground motion records is selected in this study to account for the record-to-record variability and evaluate the seismic response of the case-study structures through IDAs [65]. The set is selected using REXEL [66], considering a moment magnitude (M_w) ranging from 6 to 7, epicentral distance $R \leq 30$ km and spectrum compatibility in the range of periods between $0.2T_1$ and $2T_1$. The ground motions set is selected to match, on average, the Eurocode 8 elastic response spectrum [1] adopted for the design, considering upper and lower tolerance limits equal to 30% and 25%, respectively. A large number of zeros acceleration points (*i.e.*, 40 s) is added at the end of each record in order to allow the free vibrations to stop and to correctly capture the residual displacements. The spectral acceleration corresponding to the first vibration mode ($S_a(T_1)$) is assumed as *IM*, and the IDAs are performed by scaling each ground motion record to increasing *IM* values with a constant step of 0.1g. Figure 16(a) and (b) show the selected spectra and the scaled spectra at the ULS intensity, respectively.

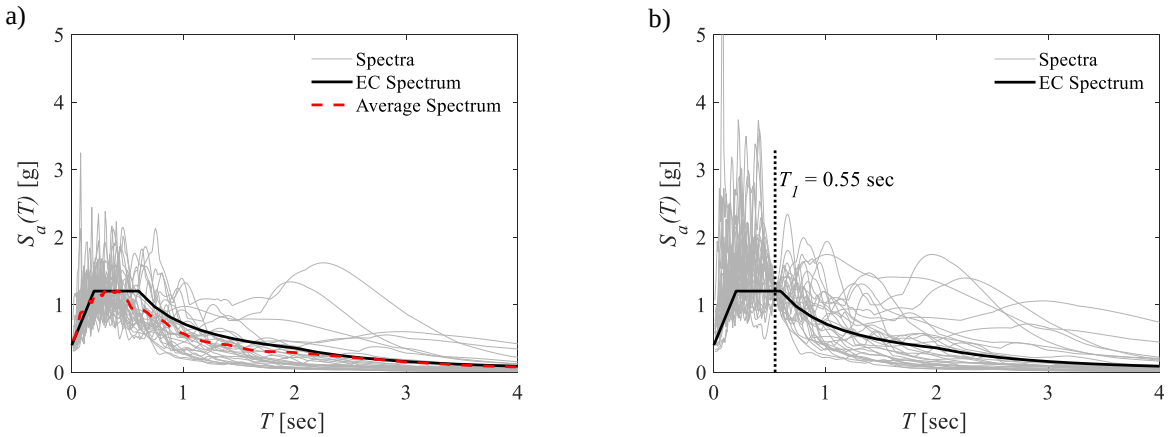

Figure 16. (a) Spectra of the selected ground motion records; (b) Spectra scaled at the ULS intensity.

5.4 *Incremental Dynamic Analyses (IDAs)*

The seismic performance of the EBF and SC-EBF is evaluated through IDAs [65]. Peak and residual interstorey drifts ($\theta_{max\text{-}peak}$ and $\theta_{max\text{-}res}$), as well as peak and residual link rotations ($\theta_{P,max\text{-}peak}$ and $\theta_{P,max\text{-}res}$), are selected as EDPs, and the results are expressed by means of the maximum values obtained among all the storey of the structures. The threshold values of the residual drifts for DS1 and DS2 suggested by the FEMA P-58 [44], corresponding respectively to $\theta_{res\text{-}DS1}$ = 0.2% and $\theta_{res\text{-}DS2}$ = 0.5% are considered to evaluate the self-centring capability of the structures. The seismic intensity is reported as dimensionless quantity, *i.e.*, IM_N, defined by the ratio between the *IM* value and the corresponding spectral acceleration at the ULS, $S_a(T_1)_{ULS}$. In this way, the IM_N intensities which identify the DLS, the ULS and the CLS limit states are equal to 0.5, 1.0 and 1.5, respectively. It is important to highlight that the vibration periods, and consequently the IM_N intensities, are the same for the EBF and SC-EBF hence allowing the comparison of the IDA results.

Figure 17 shows the results of the IDAs. The red and blue lines represent the individual IDA curves for the EBF and the SC-EBF, respectively. The results are synthesised through the 16%, 50% and 84% fractiles among all ground motions, as indicated from the bold lines (for the 50% fractile) and the filled areas (for the 16% and 84% fractiles). Additionally, to compare the seismic responses of the frames (EBF and SC-EBF), the percentage reduction (Δ) of the median values (50% fractile) is reported for the seismic intensities of interest.

Figure 17(a) and (b) show the results of the IDAs in terms of peak EDPs (*i.e.*, $\theta_{max\text{-}peak}$ and $\theta_{P,max\text{-}peak}$). Highlighted in Figure 17(b) is θ_{PR} value (*i.e.*, the design target rotation). For the $\theta_{max\text{-}peak}$ (Figure 17(a)), the 50% fractile in the EBF at the ULS and CLS levels are 1.55% and 2.79%, respectively, compared to 1.96% and 3.42% in the SC-EBF. Besides, $\theta_{P,max\text{-}peak}$ (Figure 17(b)) in the EBF experiences values equal to 0.09 *rad* and 0.17 *rad* at the ULS and the CLS, respectively, in comparison with 0.12 *rad* and 0.30 *rad* in the SC-EBF. These values show that using the SC-links increases the frame's response at peak, both in terms of interstorey drifts and link rotations. In particular, as indicated from the Δ values, an increment between 24% and 37% is observed for $\theta_{max\text{-}peak,50\%}$, while greater dispersion occurs for $\theta_{P,max\text{-}peak,50\%}$ (*i.e.*, 105% at DLS, 38% at ULS and 63% at CLS). The aforementioned results allow some observations. In particular, in the EBF $\theta_{P,max\text{-}peak}$ reached values close to θ_{PR} at the ULS according to the seismic demand in terms of link rotation provided by the seismic code [1] for designing short links, ensuring the link rotation capacity hence preventing local fracture risk in the links. Conversely, greater link rotation demand should be taken into account for the CLS. In the SC-EBF, the increment of the peak deformation parameters is a consequence of the minor dissipation capacity of the SC-EBF. This effect does not compromise the self-centring capacity of the structure but highlights the need for careful considerations in the design, accounting for the lower dissipation capacity of the system.

Figure 17(c) and (d) show the results of the IDAs in terms of residual EDPs (*i.e.*, $\theta_{max\text{-}res}$ and $\theta_{P,max\text{-}res}$). The horizontal lines indicate the values for $\theta_{res\text{-}DS1}$ and $\theta_{res\text{-}DS2}$ [44]. In the EBF the 50% fractile of $\theta_{max\text{-}res}$ (Figure 17(c)) is 0.3% and 0.4% at ULS and CLS, respectively. These values meet the threshold limit $\theta_{res\text{-}DS2}$ but are higher than $\theta_{res\text{-}DS1}$, indicating the need to realign the frame after a rare seismic event. The median value of $\theta_{P,max\text{-}res}$ (Figure 17(d)) experiences values equal to 0.02 *rad* and 0.03 *rad* at the ULS and the CLS, respectively. Conversely, for the SC-EBF the 50% fractile both in terms of $\theta_{max\text{-}res}$ and $\theta_{P,max\text{-}res}$ is almost zero for all the IM_N, ensuring the reparability of the structures without the need for realignment [44]. These results show that the introduction of the SC-links allows obtaining a significant improvement in terms of residual interstorey drifts. Besides, this is evidenced by the Δ values, which indicate a high percentage reduction for all the IM_N both in terms of $\theta_{max\text{-}res}$ and $\theta_{P,max\text{-}res}$.

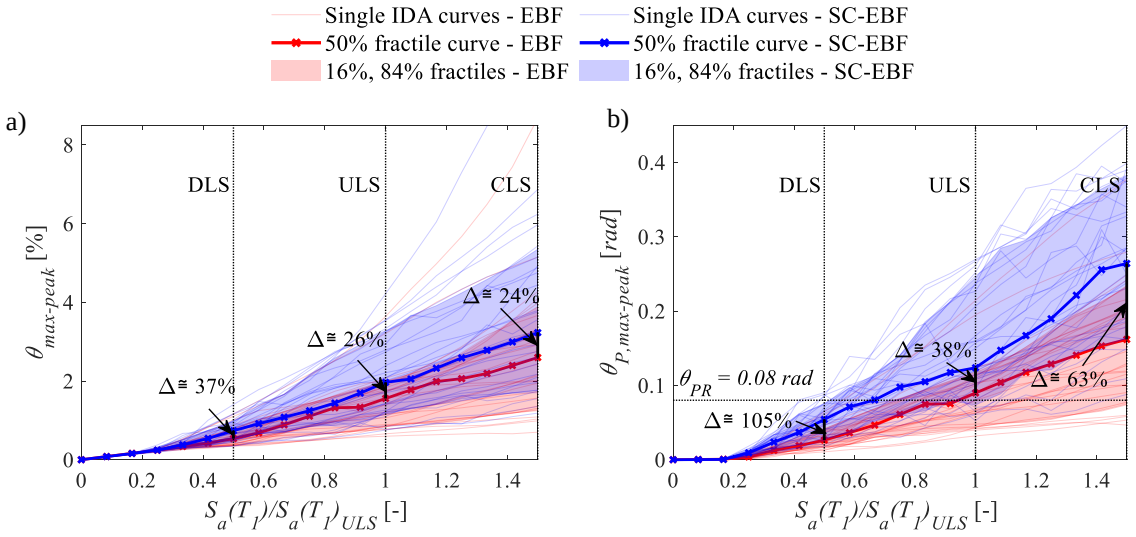

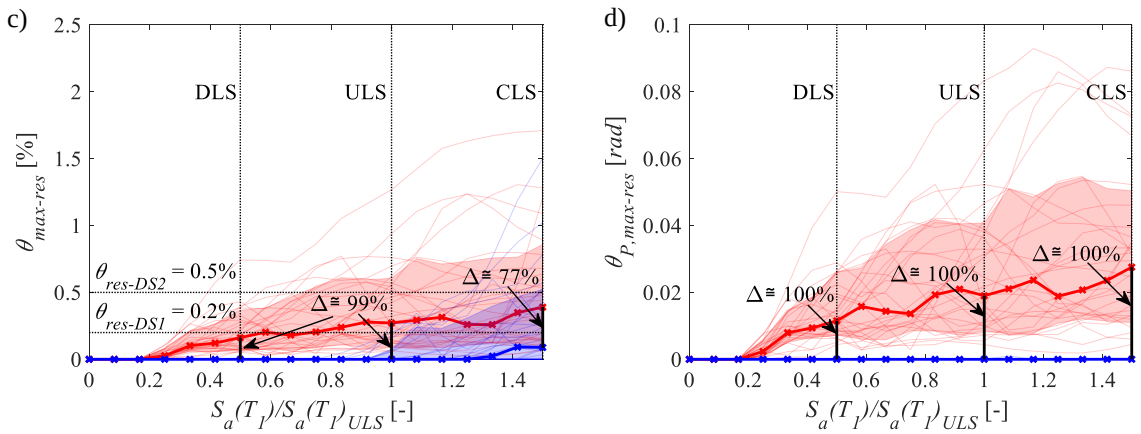

Figure 17. IDA comparison in terms of (a) peak interstorey drifts and (b) peak link rotations for the case-study frames (c) residual interstorey drifts, and (d) residual link rotations for the case-study frames.

Figure 18 shows the seismic response of the two configurations in terms of first story displacement time histories for a single ground motion record scaled at ULS (Figure 18(a)) and CLS (Figure 18(b)) intensities. The comparison of the responses for the EBF and SC-EBF shows how the proposed SC-link provides significant improvements in terms of residual drifts reduction, ensuring the reparability of the building. The figures further highlight how the peak displacement response is higher in the SC-EBF at both intensities.

Figure 19(a) and (b) show the distribution among the storeys of the peak interstorey drifts (θ_{max}) and peak link rotations ($\theta_{P,max}$) at the ULS. The 50% fractile of the aforementioned quantities among all ground motion is highlighted with bold lines (*i.e.*, red and blue bold lines for EBF and SC-EBF, respectively). The results show that the increase of both the θ_{max} and $\theta_{P,max}$ in the SC-EBF is higher at the upper storeys of the structure, while smaller increments of the aforementioned parameters are observed at the first storey. Similarly, Figure 19(c) and (d) show the distribution among the storeys of the residual interstorey drifts (θ_{res}) and the residual link rotations ($\theta_{P,res}$) at the ULS. The results show that the use of SC-links allows for eliminating the residual drifts at all the storeys.

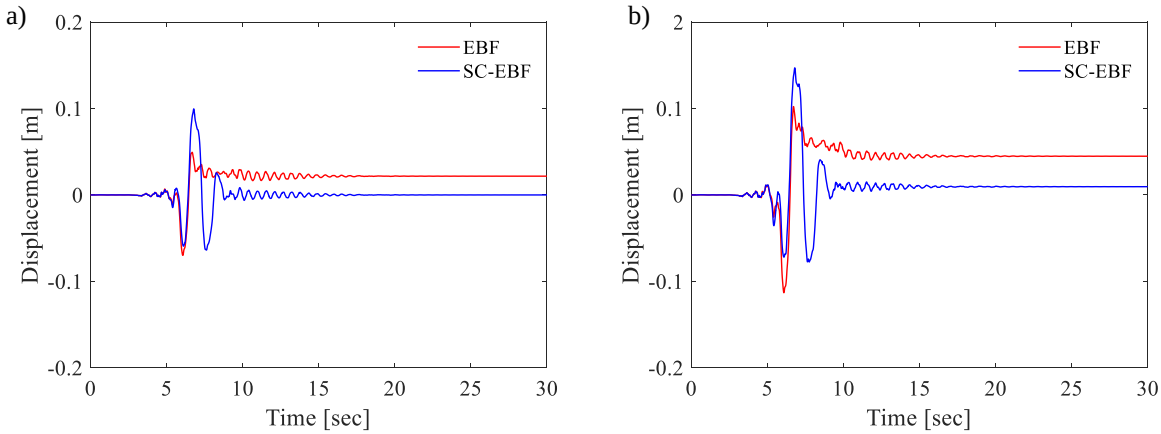

Figure 18. Comparison of the first-storey displacement time-history for a single ground motion record scaled at (a) ULS and (b) CLS intensities.

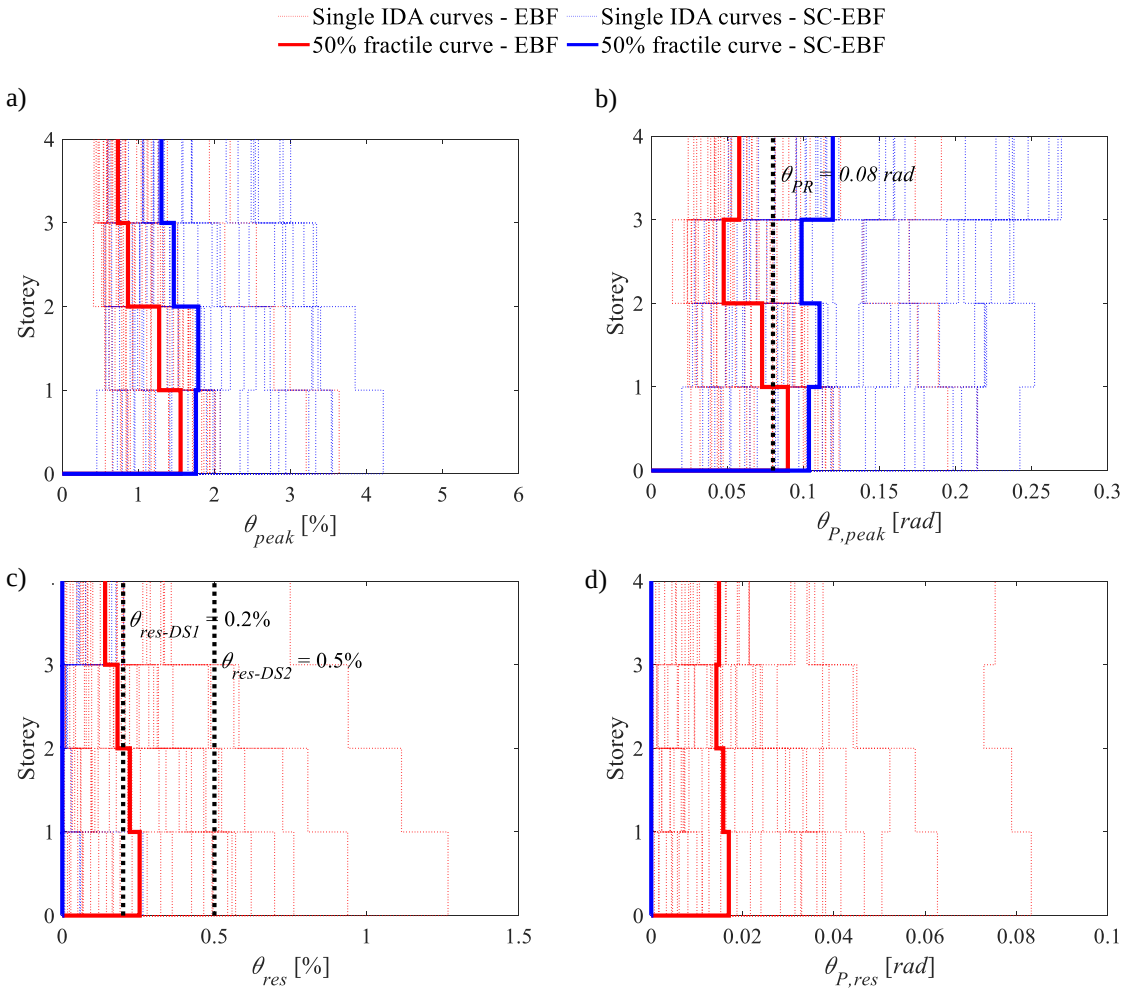

Figure 19. IDA comparison in terms of vertical profiles for (a) peak interstorey drift; (b) residual interstorey drift; (c) peak link rotation; (d) residual link rotation for the case-study frames at the ULS.

Figure 20 shows the variation of the F_{max}/F_1 ratio for all the storeys of the SC-EBF. F_{max} is the maximum longitudinal shear force registered in the SC-links during the non-linear time history analyses, and F_1 represents the design longitudinal shear force adopted for designing the SC-links. The 50% fractile among all ground motions is highlighted in the figures with solid lines, while the single IDA data are reported as cloud data.

This figure shows that at the ULS, which represents the design limit state for the SC-links, the median F_{max}/F_1 ratio is close to 1.5 at all storeys, as expected from the design assumption (F_2/F_1 ratio is limited to 1.5). Conversely, an increase in this value is observed for seismic intensity higher than the ULS. In particular, at the CLS the 50% fractile of the F_{max}/F_1 ratio is equal to 1.78, 1.88, 1.78 and 2.62, respectively, from the first to the fourth storeys. It is important to observe that high F_{max}/F_1 ratios can affect the damage-free behaviour of the SC-links, due to high longitudinal shear forces acting in the SC-links, which can result in the yielding of the T-plate, L-plates, pin connections and anchor plates. For this reason, further limitations of the F_2/F_1 ratio could be required in the design procedure to account for the strain-hardening of the SC-links.

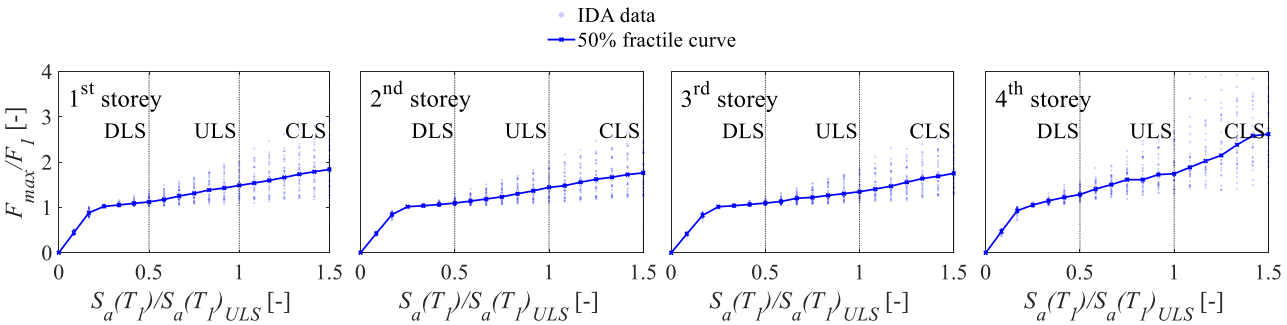

Figure 20. Evolution of the maximum longitudinal shear force acting in the SC-links (F_{max}) and link's design longitudinal shear force (F_1) ratio for SC-EBF.

6. CONCLUSIONS

This paper presents a damage-free self-centring link (SC-link) for eccentrically braced frames (EBFs). The SC-link uses post-tensioned high-strength steel bars with disk springs to control the self-centring capacity of the frame and friction devices to dissipate seismic energy. The flag-shape behaviour and the analytical equations governing the global behaviour of the connection are provided. A four-storey EBF is designed according to Eurocode 8 provisions with conventional short links and upgraded with the proposed SC-link. The third storey of the structure is extracted to develop refined 3-D finite element (FE) models in ABAQUS. The results of the 3-D FE simulations are used to investigate the local behaviour of the connection and validate the accuracy of the analytical predictions. Based on the 3-D FE modelling results, a 2-D simplified nonlinear FE model is developed in OpenSees. Non-linear static push-pull analysis and Incremental Dynamic Analysis are carried out. A set of 30 ground motion records is used to perform non-linear dynamic analyses accounting for the record-to-record variability. The seismic performances of the EBF with conventional links and the EBF with SC-links are investigated and compared. The spectral acceleration corresponding to the fundamental period of vibration is used as intensity measure (IM). Residual and peak interstorey drifts, as well as residual and peak link rotations are identified as Engineering Demand Parameters (EDPs). The results of the conventional and upgraded systems are compared, showing the influence of the SC-links on the seismic performance of the frames. The following main outcomes can be drawn: (1) the ABAQUS results show that the proposed SC-link is characterised by a damage-free behaviour and is able to restore the frame at the initial configuration, providing the flag-shape hysteretic response; (2) a good agreement is observed between the hysteretical behaviour obtained from numerical simulations and predicted by the analytical formulations; (3) the OpenSees results show that the introduction of the proposed SC-link in conventional EBF allows limiting/avoiding the residual interstorey drifts for the whole range of intensity measure values investigated, ensuring the repairability of the structures without the need for realignment; (4) the reduced dissipation capacity of the self-centring system produces an increase of the peak values of the frame responses, both in terms of interstorey drifts and link rotations. This effect does not compromise the self-centring capability of the structures (as demonstrated by the residual maximum interstorey drift and residual maximum link rotation results). However, it highlights the need to carefully consider the lower dissipation capacity of the self-centring structures in the design phase.

REFERENCES

1. EN 1998-1, Eurocode 8: Design of structures for earthquake resistance – Part 1: General rules, seismic actions and rules for buildings, *European Committee for Standardization*, Brussels.
2. ASCE/SEI 7–16, Minimum Design Loads and Associated Criteria for Buildings and Other Structures, *American Society of Civil Engineers*, 2017.
3. Freddi F., Novelli V., Gentile R., Veliu E., Andonov A., Andreev S., Greco F., Zhuleku E., Observations from the 26th November 2019 Albania Earthquake: the Earthquake Engineering Field Investigation Team (EEFIT) mission. *Bulletin of Earthquake Engineering*, **19**(5): 2013-2044, 2021.
4. Clifton G.C., Bruneau M., MacRae G.A., Leon R., Fussel A., Steel structures damage from the Christchurch earthquake series of 2010 and 2011, *Bulletin of the New Zeland Society for Earthquake Engineering*, **44**(4), 2011.
5. McCormick J., Aburano H., Nakashima M., Permissible residual deformation levels for building structures considering both safety and human elements, *14th World Conference of Earthquake Engineering*, Beijing, China, pp. 12–17, 2008.
6. Chancellor NB, Eatherton MR, Roke DA, Akbas T., Self-Centering Seismic Lateral Force Resisting Systems: High Performance Structures for the City of Tomorrow, *Buildings*, **4**: 520–548, 2014.
7. Freddi, F., Galasso, C., Cremen, G., Dall'Asta, A., Di Sarno, L., Giaralis, A., Gutiérrez- Urzúa, L.F., Málaga-Chuquitaype, C., Mitoulis S., Petrone, C., Sextos, A., Sousa, L., Tarbali, K., Tubaldi, E., Wardman, J., Woo, G., Innovations in Earthquake Risk Reduction for Resilience: Recent Advances and Challenges, *International Journal of Disaster Risk Reduction*, **60**: 102267, 2021. https://doi.org/10.1016/j.ijdrr.2021.102267.
8. Fang C., Wang W., Qiu C., Hu S., MacRae G.A., Eatherton M.R. Seismic resilient steel structures: A review of research, practice, challenges and opportunities. *Journal of Constructional Steel Research*, **191**: 107172, 2022.
9. Shen Y., Freddi F., Li Y., Li J. Parametric experimental investigation of unbonded post-tensioned reinforced concrete bridge piers under cyclic loading. *Earthquake Engineering & Structural Dynamics*, **51**: 3479–3504, 2022. DOI: 10.1002/eqe.3732
10. Christopoulos C., Filiatrault A., Uang C. -M., Folz B., Post-tensioned energy dissipating connections for moment-resisting steel frames, *Journal of Structural Engineering*, **128**(9), 1111–1120, 2002.
11. Garlock M.M., Sause R., Ricles J.M., Behavior and Design of Post-tensioned Steel Frame Systems, *Journal of Structural Engineering*, **133**, 389–399, 2007.
12. Khoo H.H., Clifton C., Butterworth J., MacRae G., Gledhill S., Sidwell G. Development of the self-centering sliding hinge joint with friction ring springs, *J. Constr. Steel Res.*, **78**: 201–211, 2012.

13. Vasdravellis G., Karavasilis T.L., Uy B., Large-Scale Experimental Validation of Steel Posttensioned Connections with Web Hourglass Pins, *Journal of Structural Engineering*, **139**, 1033–1042, 2013.
14. Freddi F., Dimopoulos C., Karavasilis T.L., Rocking damage-free steel column base with friction devices: design procedure and numerical evaluation, *Earthquake Engineering & Structural Dynamics*, **46**(14), 2281-2300. DOI: 10.1002/eqe.2904.
15. Freddi F., Dimopoulos C., Karavasilis T.L., Experimental evaluation of a rocking damage-free steel column base with friction devices. *Journal of Structural Engineering*, **146**(10), 04020217, 2020.
16. Latour M., Rizzano G., Santiago A., Da Silva L., Experimental response of a low yielding, self-centering, rocking CB joint with friction dampers, *Soil Dynamic and Earthquake Engineering*, **116**, 580–592, 2019.
17. Elettore E., Freddi F., Latour M., Rizzano G., Design and analysis of a seismic resilient steel moment resisting frame equipped with damage-free self-centering column bases, *Journal of Constructional Steel Research*, **179**, 106543, 2021.
18. Elettore E., Lettieri A., Freddi F., Latour M., Rizzano G., Performance-Based Assessment of Seismic-Resilient Steel Moment Resisting Frames Equipped with Innovative Column Bases Connections, *Structures*, **32**, 1646–1664, 2021.
19. Elettore E., Freddi F., Latour M., Rizzano G., Parametric study and finite element analysis of self-centring steel column bases with different structural properties, *Journal of Constructional Steel Research*, **199**: 107628, 2022. https://doi.org/10.1016/j.jcsr.2022.107628
20. Pieroni L., Freddi F., Latour M., Effective placement of Self-Centering Damage-Free Connections for Seismic-Resilient Steel Moment Resisting Frames, *Earthquake Engineering & Structural Dynamics*, **51**(5): 1292–1316, 2022. DOI: 10.1002/eqe.3615
21. Pieroni L., Di Benedetto S., Freddi F., Latour M., Genetic Algorithm for the optimal placement of Self-Centering Damage-Free joints in steel MRFs, *Journal of Constructional Steel Research,* **197**: 107489, 2022. https://doi.org/10.1016/j.jcsr.2022.107489.
22. Ke K., Zhou X., Zhang H., Yam M.C.H., Guo L., Chen Y., Performance-based-plastic-design of damage-control steel MRFs equipped with self-centring energy dissipation bays, *Journal of Constructional Steel Research,* **192**: 107230, 2022. https://doi.org/10.1016/j.jcsr.2022.107230.
23. Ke K., Zhou X., Zhu M., Yam M.C.H., Wang Y., Zhang H., Seismic evaluation of industrial steel moment resisting frames with shape memory alloys using performance-spectra-based method, Journal of Building Engineering, **48**: 103950, 2022. https://doi.org/10.1016/j.jobe.2021.103950.
24. Christopoulos C., Tremblay R., Kim H.-J., Lacerte M., Self-Centering Energy Dissipative Bracing System for the Seismic Resistance of Structures: Development and Validation, *Journal of Structural Engineering*, **134**, 96–107, 2008.
25. Braconi A., Morelli F., Salvatore W. Development, design and experimental validation of a steel self-centering device (SSCD) for seismic protection of buildings. *Bulletin of Earthquake Engineering*, **10**, 1915–1941, 2012. https://doi.org/10.1007/s10518-012-9380-9.
26. Erochko J., Christopoulos C., Tremblay R. Design and testing of an enhanced elongation telescoping self-centering energy-dissipative brace, *J. Struct. Eng.* **141**(6): 04014163, 2015.
27. Chou C., Tsai W., Chung P. Development and validation tests of a dual-core selfcentering sandwiched buckling-restrained brace (SC-SBRB) for seismic resistance, *Eng. Struct.*, **121**: 30–41, 2016.
28. Xu L., Fan X., Li Z. Experimental behavior and analysis of self-centering steel brace with pre-pressed disc springs, *J. Constr. Steel Res.*, **139**: 363–373, 2017.
29. Wang W., Fang C., Zhao Y., Sause R., Hu S., Ricles J. Self-centering friction spring dampers for seismic resilience, *Earthquake Eng. Struct. Dynam.*, **48**(9): 1045–1065, 2019.
30. O'Reilly G.J., Goggins J., Experimental testing of a self-centring concentrically braced steel frame, *Engineering Structures* 111521, 2021. https://doi.org/10.1016/j.engstruct.2020.111521.
31. Fujimoto M., Aoyagi T., Ukai K., Wada A., Saito K., Structural characteristics of eccentric k-braced frames. *Architectural Institude of Japan*, **195**, 39-49, 1972.
32. Tanabashi R., Naneta K., Ishida T., On the rigidity and ductility of steel bracing assemblage, *5th World Conference of Earthquake Engineering* (IAEE), Rome, Italy, 1974.
33. Roeder C.W., Popov E.P., Inelastic behavior of eccentrically braced steel frames under cyclic loading, Berkeley Earthquake Engineering Research Center. University of California, Report No. UCB/EERC-77/18, Berkeley, CA, USA, 1977.
34. Hielmstad D.K., Popov E.P., Characteristics of eccentrically braced frames, *Journal of Structural Engineering*, **110**(2), 340-353, 1984.
35. Okazaki T., Arce G., Ryu H.-C., Engelhardt M.D. Experimental study of local buckling, overstrength, and fracture of links in eccentrically braced frames. *Journal of Structural Engineering*, **131**(10): 1526 - 1535, 2005.

36. Gutiérrez-Urzúa L.F., Freddi F., Di Sarno L., Comparative Analysis of Code Based Approaches for the Seismic Assessment of Existing Steel Moment Resisting Frames, *Journal of Constructional Steel Research*, **181**, 106589, 2021. https://doi.org/10.1016/j.jcsr.2021.106589.
37. Costanzo S., D'Aniello M., Landolfo R., Seismic design rules for ductile Eurocode-compliant two-storey X concentrically braced frames, *Steel and Composite Structures*, **36**, 273-291, 2020.
38. Clifton G.C., Nashid H., Ferguson G., Hodgson M., Seal C., Performance of Eccentrically Braced Framed Buildings in The Christchurch Earthquake Series of 2010/2011, *15th World Conference on Earthquake Engineering*, 2012.
39. Stratan A., Dubina D., Bolted links for eccentrically braced steel frames, Proceedings of the Fifth AIS/ECCS International Workshop Connections in Steel Structures V. Behaviour, Strength and Design, Delft University of Technology, Netherlands, June 3-5, 2004.
40. Mansour N., Christopoulos C., Tremblay R., Experimental validation of replaceable shear link for eccentrically braced frames, *Journal of Structural Engineering*, **137**(10), 1141-1152, 2011.
41. Khan M., Clifton G.C., Proposed development of a damage-resisting eccentrically braced frames with rotational active links, *Bulletin of the New Zealand Society for Earthquake Engineering*, **44**(2), 2011.
42. Bozkurt M.B., Topkaya C., Replaceable links with gusseted brace joints for eccentrically braced frames, *Soil Dynamics and Earthquake Engineering*, **115**, 305-318, 2018.
43. Bozkurt M.B., Azad S.K., Topkaya C., Development of detachable replaceable links for eccentrically braced frames, *Earthquake Engineering & Structural Dynamics*, **48**, 1134-1155, 2019.
44. FEMA P58-1. Seismic Performance Assessment of Buildings. Volume 1 – Methodology. Applied Technology Council, 2012.
45. Dubina D., Stratan A., Dinu F., Dual high-strength steel eccentrically braced frames with removable links, *Earthquake Engineering & Structural Dynamics*, **37**, 1703-1720, 2008.
46. Ioan A., Stratan A., Dubina D., Poljansek M., Molina F.J., Taucer F., Pegon P., Sabau G., Experimental validation of re-centring capability of eccentrically braced frames with removable links, *Engineering Structures*, **113**, 335-346, 2016.
47. Cheng C.T., Hsu C.H., Seismic behaviour of self-centering designed eccentrically braced frames, *15th World Conference on Eartquake Engineering*, Lisboa, 2012.
48. Tong L., Zhang Y., Zhou X., Keivan A., Li R., Experimental and Analytical Investigation of D-Type Self-Centering steel eccentrically braced frames with replaceable hysteretic damping devices, *Journal of Structural Engineering*, **145**(1), 2019.
49. Al-Janabi Q., Yang T.Y., Performance assessment of novel self-centring friction-based eccentrically braced frames, *Engineering Structures*, **241**, 112456, 2021.
50. Rezvan P., Zhang Y., Nonlinear seismic performance study of D-type self-centring eccentric braced frames with sliding rocking link beams, *Earthquake Engineering Structural Dynamics*, 1-21, 2021.
51. Xu X., Zhang Y., Luo, Y. Self-centering eccentrically braced frames using shape memory alloy bolts and post-tensioned tendons, *Journal of Constructional Steel Research*, **125**, 190-204, 2016.
52. Askariani S. S., Garivani S., Hajirasouliha I., Soleimanian N., Innovative self-centring systems using shape memory alloy bolts and energy dissipating devices, *Journal of Constructional Steel Research*, **190**, 107-127, 2022.
53. Xu X., Zheng Y., Luo Y., Self-centering links using post-tensioned composite tendons, *Advances in Structural Engineering*, **21**(9), 1302-1312, 2017.
54. Mirzai N.M., Attarnejad R., Hu J.W., Experimental investigation of smart shear dampers with re-centring and friction devices, *Journal of Building Engineering*, **35**, 102018, 2021.
55. ABAQUS – Analysis User's Manual Version 6.17, Abaqus Inc., 2017.
56. Mazzoni S. McKenna F. Scott MH, Fenves GL. OpenSEES: Open System for earthquake engineering simulation, *Pacific Earthquake Engineering Research Centre (PEER)*, University of California, Berkley, CA, 2009. Available at: http://opensees.berkeley.edu.
57. Ramhormozian S., Clifton G.C., MacRae G.A., Davet G.P., Stiffness-based approach for Belleville springs use in friction sliding structural connections, *Journal of Constructional Steel Research*, **138**, 340-356, 2017.
58. Ramhormozian S., Clifton G.C., MacRae G.A., Davet G.P., Khoo H.H., Experimental studies on Belleville springs use in the sliding hinge joint, *Journal of Constructional Steel Research*, **159**, 81-94, 2019.
59. Chou C.C., Tsai K.C., YangW.C. Self-centering steel connections with steel bars and a discontinuous composite slab. *Earthquake Engineering Structural Dynamics*, **38**, 403–422, 2009.
60. Kasai K., Han X., New EBF design method and applications: Redesign and analysis of US-Japan EBF, *2nd International Conference on Behaviour of Steel Structures in Seismic Areas* (STESSA), 1997.
61. EN 1998-1, Eurocode 3: Design of steel structures – Part 1-8: Design of joints, *European Committee for*

Standardization, Brussels.

62. Cavallaro G.F., Francavilla A.B., Latour M., Piluso v., Rizzano G., Cyclic behaviour of friction materials for low yielding connections, *Soil Dynamics and Earthquake Engineering*, **114**, 404-423, 2008.
63. Della Corte G., D'Aniello M., Mazzolani F.M., Inelastic response of shear links with axial restraints: numerical vs. analytical results, *Proceedings of 5th international conference on advances in steel structures*, ICASS 2007, Singapore, p. 651-656, 2007.
64. Della Corte G., D'Aniello M., Landolfo R., Analytical and numerical study of plastic overstrength of shear links, *Journal of Constructional Steel Research*, **82**, 19-32, 2013.
65. Vamvatsikos D., Cornell CA., Incremental Dynamic Analysis, Earthquake Engineering Structural Dynamics, **31**(3), 491-514, 2002.
66. Iervolino I., Galasso C., Cosenza E., REXEL: Computer aided record selection for code-based seismic structural analysis, *Bulletin of Earthquake Engineering*, **8**, 339-362, 2010.